NASA
Technical
Paper
2159

July 1983

Wall-Temperature Effects on the Aerodynamics of a Hydrogen-Fueled Transport Concept in Mach 8 Blowdown and Shock Tunnels

Jim A. Penland,
Don C. Marcum, Jr.,
and Sharon H. Stack

NASA

25th Anniversary
1958-1983

NASA
Technical
Paper
2159

1983

Wall-Temperature Effects on the Aerodynamics of a Hydrogen-Fueled Transport Concept in Mach 8 Blowdown and Shock Tunnels

Jim A. Penland,
Don C. Marcum, Jr.,
and Sharon H. Stack
Langley Research Center
Hampton, Virginia

NASA
National Aeronautics
and Space Administration

**Scientific and Technical
Information Branch**

SUMMARY

Results are presented from two separate tests on the same blended wing-body hydrogen-fueled transport model at a Mach number of about 8 and a range of Reynolds numbers (based on theoretical body length) of 0.597×10^6 to about 156.22×10^6. Tests were made in a conventional hypersonic blowdown tunnel and a hypersonic shock tunnel at angles of attack of -2° to about 8°, with an extensive study made at a constant angle of attack of 3°. The model boundary-layer flow varied from laminar at the lower Reynolds numbers to predominantly turbulent at the higher Reynolds numbers. Model wall temperatures and stream static temperatures varied widely between the two tests, particularly at the lower Reynolds numbers. For the blowdown-tunnel tests, the wall temperature was about 860°R and the stream static temperature was about 100°R; for the shock-tunnel tests, the wall temperature was about 540°R and the stream static temperature was 200°R to 300°R. These temperature differences resulted in marked variations of the axial-force coefficients between the two tests, due in part to the effects of induced pressure and viscous interaction variations. The normal-force coefficient was essentially independent of Reynolds number. Current theoretical computer programs and basic boundary-layer theory were used to study the effects of wall temperature, static temperature, and Reynolds number.

INTRODUCTION

The interpretation and application of aerodynamic test data from conventional wind tunnels and shock facilities in the determination of full-scale aerodynamic performance of a particular design are the primary goal of configuration testing. This is accomplished by selecting a design having sufficient volume to house the required fuel and payload, adequate wing area for a safe landing, and a shape based on available theory, published data, and experience. Such a configuration was the liquid-hydrogen-fueled hypersonic transport concept, figure 1, that was extensively tested through a wide Reynolds number range in a shock tunnel and reported in reference 1.

The purpose of this paper is to report the results of further free-transition tests on the same model of reference 1 in a conventional hypersonic blowdown wind tunnel at the same Mach number through a sufficiently wide Reynolds number range to allow the boundary layer to vary from essentially all laminar to predominantly turbulent, to compare the data from the blowdown tunnel with the data from the shock tunnel, and to analyze the results.

The major differences existing between tests in the two tunnels were the ratios of model wall temperature to stagnation temperature and the stream static temperatures. The shock-tunnel data were taken with a relatively low model wall temperature and a relatively high stream static temperature, whereas the conventional wind-tunnel data were taken with a high model wall temperature and a low stream static temperature.

Presentation of results includes a comparison between all experimental longitudinal force and moment coefficients measured in a conventional blowdown hypersonic tunnel and those measured in a hypersonic shock tunnel; experimental data are then compared with theoretical predictions made with the Mark III Gentry Hypersonic

Arbitrary-Body Aerodynamics Computer Program (GHABAP). (See ref. 2.) The experimental data were obtained at a Mach number of about 8 through a Reynolds number range (based on theoretical model body length) from about 0.597×10^6 to about 156.22×10^6. The model boundary-layer flow was laminar at the lower Reynolds numbers and predominantly turbulent at the higher Reynolds numbers. The angle-of-attack range was from -2° to about 8°.

The results of an extensive study of data at a constant angle of attack of 3° are presented. Included in the study is a comparison of experimental data with calculations from the GHABAP (ref. 2), an estimation of the inviscid pressure forces by extrapolation of axial-force data to very high Reynolds numbers, and an improved method of axial-force prediction under laminar-flow conditions by evaluating the induced pressure effects, including viscous interaction, through use of the calculated displacement boundary-layer thickness distributions.

Blowdown-tunnel and shock-tunnel calibrations are presented in appendix A, a discussion of the boundary layer and laminar skin friction as affected by the wall and stream static temperatures is presented in appendix B, and a presentation of the effects of model location and test time on force data recorded in an axially symmetric hypersonic blowdown tunnel is presented in appendix C.

SYMBOLS

A reference area, area of wing including fuselage intercept, 70 in^2

C $= \dfrac{T_1 \mu'}{T' \mu_1}$

C_A axial-force coefficient

C_D drag coefficient, $\dfrac{D}{q_\infty A}$

C_F average skin-friction coefficient

C_f local skin-friction coefficient

C_L lift coefficient, $\dfrac{L}{q_\infty A}$

C_m pitching-moment coefficient, $\dfrac{M_Y}{q_\infty A \bar{c}}$

C_N normal-force coefficient, $\dfrac{F_N}{q_\infty A}$

C_p pressure coefficient

C_{p_A} axial pressure coefficient

c wing chord

$\bar{c}$ mean aerodynamic chord

c_{cl}	wing centerline root chord
c_r	exposed wing root chord
D	drag, $F_N \sin \alpha + F_A \cos \alpha$
F_A	axial force along X-axis (positive direction is -X)
F_N	normal force along Z-axis (positive direction is -Z)
L	lift, $F_N \cos \alpha - F_A \sin \alpha$
L/D	lift-drag ratio
l	reference length (theoretical length of model fuselage), 25.92 in. (see fig. 1)
M	Mach number
M_Y	moment about Y-axis
N_{Pr}	Prandtl number
P	pressure
q_∞	free-stream dynamic pressure
R	Reynolds number
R_l	Reynolds number based on theoretical fuselage length, free-stream conditions
R_x	Reynolds number based on distance from leading edge
T	temperature
T'	reference temperature (see appendix B)
V	volume
X	distance from beginning of boundary layer
Y/b	percent exposed wing semispan
α	angle of attack
δ^*	boundary-layer displacement thickness
γ	ratio of specific heat
μ	dynamic viscosity
μ'	dynamic viscosity based on reference temperature

Subscripts:

aw	adiabatic wall
B	body
IP	induced pressure
Inv	inviscid
LE	leading edge
max	maximum
min	minimum
o	stagnation condition
p	planform
TE	trailing edge
unit	per unit of length
VI	viscous interaction
W	wing
w	wall condition
x	local distance from leading edge or from beginning of boundary layer
1	local
∞	stream condition

Abbreviations:

Cal.	calculated
GHABAP	Gentry Hypersonic Arbitrary-Body Aerodynamics Program (Mark III version)
Inv.	inviscid
LRC	Langley Research Center
t.p.	tangent point (see fig. 2)

Fuselage dimensions detailed in table II and figure 2:

X/ι	body station, in percent theoretical fuselage length
X	distance from nose of fuselage to cross section

H	height of fuselage
A	distance between reference line and top of fuselage
rad. B	radius of fuselage bottom
rad. T	radius of fuselage top
rad. US	radius of strake upper surface
rad. LS	radius of strake lower surface
rad. E	radius of fuselage side
Sd	distance from bottom of fuselage to strake leading edge
SW	distance from side of fuselage to strake leading edge
rad. W	radius of fairing from fuselage to wing

TEST CONFIGURATION

The test model was the 1/150-scale hypersonic transport concept of reference 1 and is shown in figure 1. The fuselage cross-section design was semielliptical with a width-height ratio of 2 to 1; the cross-sectional area was expanded from the nose to a maximum at the 0.66 body station according to the Sears Haack volume distribution equations for minimum drag bodies of reference 3 and converged to zero at station 1.00. Strakes were added to improve the hypersonic lifting capability of this voluminous component. The fuselage was blended with the strakes and the wing to reduce adverse component interference effects. (Details of the configuration tested are shown by the solid lines in fig. 1.) The vertical tail and engine were not installed for the present tests. The fuselage cross-sectional design scheme is shown in figure 2. All design curves were circular arcs to facilitate fabrication. The overall geometric characteristics of the model are presented in table I and the detailed fuselage dimensions illustrated in figure 2 are presented in table II. The model was constructed entirely of 4130 steel to provide maximum strength in an annealed condition to withstand the high loads imposed on the model during the shock-tunnel tests. The model fuselage was machined to accept a three-component strain-gage balance and three accelerometers to measure aerodynamic forces, moments, and accelerations for the shock-tunnel tests. A six-component strain-gage balance was utilized for the blowdown wind-tunnel tests.

PRESENTATION OF RESULTS

The results of wind-tunnel and shock-tunnel tests at $M \approx 8$ on a wing-body model of a hypersonic transport concept are presented in the following figures:

APPARATUS AND TESTS

Langley Mach 8 Variable-Density Tunnel

The Langley Mach 8 Variable-Density Tunnel consists of an axially symmetric nozzle with contoured walls, has an 18-inch-diameter test section, and operates on a blowdown cycle. The tunnel-wall boundary-layer thickness, and hence the free-stream Mach number, is dependent upon the stagnation pressure. For these tests the stagna-

tion pressure was varied from about 128 to 2835 psia and the stagnation temperature was varied from about 1135°R to 1480°R to avoid air liquefaction and the supersaturated region as defined in reference 4. The resulting Reynolds number varied from about 0.637×10^6 to 11.0×10^6 per foot. Dry air was used for all tests to avoid any condensation effects. The calibration of this tunnel for the present tests is presented in figures 9 to 11 and discussed in appendix A. The model was tested in the Mach 8 Variable-Density Tunnel on a sting-mounted internal six-component water-cooled strain-gage balance. This combination was injected into the hypersonic flow after the blowdown cycle had begun and retracted before the cycle was stopped. Tests were made with free transition at a fixed angle of attack, and the final data were corrected for sting deflection. The moment reference station was placed at 6.15 percent $\bar{c}$, 0.566l. (See fig. 1.) Tests were conducted through an angle-of-attack range of about -1° to 7° at zero sideslip angle. The base pressures were measured for all tests, and the axial force was corrected to a condition of free-stream static pressure on the base.

Calspan Hypersonic Shock Tunnel

The Calspan 96-Inch Hypersonic Shock Tunnel, described in reference 5, employs a reflected shock to process air to conditions suitable for supplying an axially symmetric convergent-divergent hypersonic nozzle. The shock-processed air is expanded through a contoured nozzle, having interchangeable throats, to the desired test conditions at the 24-inch exit diameter. Test time varied with conditions up to about 13 milliseconds duration. For the shock-tunnel tests the stagnation pressure varied from about 337 psia to 18 650 psia, and stagnation temperature varied from about 691°R to 3973°R to avoid liquefaction and to tailor the wide test Reynolds number range at a Mach number of approximately 8. The Reynolds number per foot varied from about 0.276×10^6 to 72.3×10^6 for the shock-tunnel tests. Some of the higher stagnation temperatures were utilized at the lower stagnation pressures to help obtain the lower Reynolds numbers by increasing viscosity. Stagnation pressure, temperature, and Mach number are plotted with Reynolds number in figure 12 and are discussed in appendix A for all shock-tunnel tests. Tests were conducted in unsaturated air where the lowest test static temperature was 127.8°R; thus, as defined in reference 4, all data were taken well outside the supersaturated region. The model was mounted on a three-component strain-gage balance just downstream of the contoured nozzle exit at a fixed angle of attack for all tests, and the final data were corrected for sting deflection. The free-stream Mach number was determined from pitot pressures measured for each test run by means of piezoelectric crystal pressure transducers mounted in the test section. Tests were made with free transition, and base-pressure corrections were applied as described in the previous section on the blowdown tunnel.

THEORETICAL METHODS

The theoretical studies made in the present report consist of, first, computerized calculations predicting the various longitudinal aerodynamic coefficients at appropriate flow conditions for angles of attack up to 10° and, second, a detailed investigation of the normal and axial forces with variation in Reynolds number at a constant angle of attack of 3°, for which both the high-speed computer and desk-top calculators were utilized to evaluate the induced pressure effects on axial-force coefficients.

Inviscid Aerodynamics

The theoretical studies made major use of the Mark III Gentry Hypersonic Arbitrary-Body Aerodynamics Program (GHABAP). (See ref. 2.) The aircraft configuration was divided into approximately 800 elements, as shown in figure 3, for the calculation of both the inviscid and viscid aerodynamics. This program has available a variety of optional inviscid pressure-distribution calculation methods for both the impact flow and the shadow flow regions, which may be arbitrarily applied to individual model panels. Various methods and distributions were tried on the present configuration including the tangent-cone, tangent-wedge, and the shock-expansion methods for the impact flow regions while using the Prandtl-Meyer expansion from free stream to all shadow regions. The most successful combination was found to be the use of the tangent-cone pressure distribution on the forward fuselage and strakes ahead of the wing-fuselage junction and the tangent-wedge method on the wings and that portion of the fuselage aft of the wing-fuselage junction. This choice of pressure-distribution methods gave normal- and axial-force coefficients on the complete configuration that were essentially the same as those predicted by the use of the tangent-cone option on the fuselage and the shock-expansion option on the wings and strakes, as presented in reference 1, but gave much more realistic pitching-moment coefficients. The difference between the estimated pitching moments calculated by the methods of reference 1 and those calculated by the present methods was in excess of 10-percent static margin. This compromise in selection of inviscid pressure-distribution calculation methods is reasonable when consideration is given to the flattened conical shape of the forward fuselage and to the relatively small average thickness ratio of the aft blended wing-body cross section. Wing and fuselage leading-edge axial-force contributions were assessed from the results of the circular-cylinder study of reference 6. A base pressure coefficient of $-1/M^2$ (ref. 7) was assumed to exist on the blunt-wing trailing edge.

Skin Friction

Laminar skin friction was calculated within the GHABAP by the T'-theory (the reference-temperature method of Monaghan in ref. 8). A discussion of this reference-temperature calculation is presented in appendix B. Although the magnitude of the laminar skin friction is relatively insensitive to variations of Prandtl number and Mach number, it is sensitive to wall and local stream temperatures. For a given local stream temperature of 100°R, figure 13(a) shows that the skin friction may be expected to decrease somewhat with increasing Mach number but to decrease markedly with wall temperature. For the given hypersonic Mach number of 8, figure 13(b) shows that the laminar skin friction will decrease with increases in the ratio of wall temperature to local temperature or in stream static temperature or in both.

Turbulent skin friction was calculated within the GHABAP by the method of Spalding and Chi (ref. 9).

Induced Pressure

The buildup of a laminar boundary layer on an aerodynamic surface effectively alters the surface contour; consequently, the resulting airflow is rerouted and the surface pressure distribution is changed. Two methods of accounting for this laminar boundary-layer induced pressure were utilized.

The first method used the induced-pressure option available in the GHABAP to provide estimates for comparisons between theory and experiment with angle of attack, figure 4, and with Reynolds number at a constant angle of attack, figure 5.

The second, or present, method used detailed two-dimensional boundary-layer induced pressure estimates made for the exposed wing panels and for the fuselage and strakes at a constant angle of attack of 3° for the low Reynolds number laminar test region below $R = 10 \times 10^6$. This method is detailed as follows. The boundary-layer displacement thickness distribution was calculated for both the upper and lower surfaces of the wing and the fuselage-strake combination, taking into account the wedge-slab-wedge airfoil section of the wing, the fuselage contours, and the resulting variation of local flow conditions by the methods of reference 8. (See appendix B.) The wall temperatures were taken as 540°R for the shock-tunnel tests and 860°R for the blowdown tunnel tests, and a Prandtl number was assumed as 0.68. The variation of displacement boundary-layer thickness on a flat plate with Prandtl number and a comparison of calculations by the methods of reference 8 with a more exact method of reference 10 is presented in figure 16 and discussed in appendix B. The local slope of the displacement boundary-layer profile (figs. 17 and 18) was determined analytically at longitudinal stations, and new pressure distributions were calculated from these boundary-layer displacement thickness contours on both wing and fuselage surfaces using a tangent-wedge approximation based on stream Mach number. The difference in the integrated pressure distribution obtained by this method and the inviscid value given by the GHABAP was considered the present induced pressure increment. As an example, a plot of the pressure distributions on the wing are shown in figure 19. The new induced pressure distributions vary for $R_{unit} = 0.66 \times 10^6$ per foot and $T_w = 860°R$, from as high as 20 to 60 times the inviscid pressures immediately downstream of the leading edge for the bottom and top forward wing surfaces, respectively, to only 1.2 to 1.5 times the inviscid pressures at the wing trailing edge. Similar pressure distributions were calculated for the fuselage-strake combination. No estimates of turbulent boundary-layer induced pressures were made.

Viscous Interaction

The large induced pressure gradient (falling pressures) discussed in the preceding section has an adverse effect on the laminar skin friction and is hereafter referred to as viscous interaction. As with the induced pressure calculations, two methods were utilized to account for this viscous interaction. The first method used the GHABAP which normally tabulates the laminar skin friction in combination with an estimate of the viscous interaction. For the present analysis, this program was modified to tabulate the skin friction without the viscous-interaction increment. The increment of viscous interaction was therefore the difference between the original and the modified computer-program results. These increments were used in combination with the induced pressure increment and the leading-edge and trailing-edge drag in figure 4 and were shown separately in figure 5.

The second or present method to account for the increase in C_F due to the induced pressure gradient used the methods of reference 11 which assumed a boundary-layer velocity profile similar to those of incompressible flow and a power-law distribution of the self-induced pressure gradient. The variation of the calculated pressure distributions with distance from the leading edge was compared with the equation $P \propto X^n$ to determine the value of n that would best match the pressure-distribution curve, and a skin-friction correction coefficient was obtained from a chart of the coefficient versus n for various values of wall temperature (ref. 11).

A further-required correction was a function of the ratio of local pressure to stream pressures at the trailing edge. As with the induced pressures, the differences in the calculated values of skin friction with induced pressures (favorable pressure gradient) on the exposed surfaces by the methods of reference 11 and those values from the GHABAP without viscous interaction were considered to be the present values of viscous interaction or the incremental skin friction due to induced pressure. The present estimate of the total axial-force coefficient for the configuration at any given flow condition is therefore the sum of the inviscid and skin-friction coefficients provided by the GHABAP plus leading-edge bluntness drag, wing trailing-edge base drag, incremental values of induced pressure, and viscous interaction, i.e., the skin friction due to induced pressure gradient. Because these increments are dependent on the boundary-layer displacement thickness distribution, which (like the laminar skin friction) is a function not only of Reynolds number but also of the ratio of wall temperature to local temperature, there was a noticeable variation between data recorded in the shock tunnel with a cold-wall model and data from the blowdown tunnel with a hot-wall model. Leading-edge bluntness further contributes to the induced pressure effects, as pointed out in an early study (ref. 12), but these effects were not evaluated for the present configuration studies. No estimates of the viscous interaction were made for turbulent boundary-layer conditions.

RESULTS AND DISCUSSION

Comparison of Blowdown-Tunnel Data and Shock-Tunnel Data and Comparison of Data With Theoretical Estimates

Experimental longitudinal aerodynamics of a wing-body configuration through an angle-of-attack range from a conventional blowdown wind tunnel and a shock tunnel are compared in figure 4, along with theoretical estimates from the GHABAP. Tests were conducted in the blowdown tunnel through the widest possible Reynolds number range, and an effort was made to match those Reynolds numbers of the shock-tunnel tests. It was not possible to match the extreme Reynolds numbers (0.597×10^6 and 156.22×10^6) of the shock-tunnel tests because of the excessively thick tunnel-wall boundary layers at the lower Reynolds numbers and a design stagnation pressure limit at the higher Reynolds numbers. Therefore, there were four test Reynolds numbers from both facilities that were comparable with each other and with theory, and there were two extreme Reynolds numbers from the shock tunnel that were comparable with theory. Many tests were made in both facilities at a constant angle of attack of 3° and will be discussed subsequently.

Normal force.- It may be seen from figure 4(a) that the experimental normal-force coefficient varies only slightly between test facilities and/or with Reynolds number. Some scatter exists; but considering that each data point shown was the result of a separate wind-tunnel test made at a different time, it is not severe. The theory shows good predictions both for the trend and magnitude, particularly at possible cruise angles of attack, i.e., 2° to 5°. The small variations between normal-force predictions at the high and low Reynolds numbers are due to the variation in free-stream Mach number with tunnel stagnation pressure. At $M \approx 8$ it may be concluded that there was a minimal variation of normal-force coefficient with Reynolds number or with test facilities - although there were large variations in model surface temperatures and stagnation temperatures between the blowdown tunnel and the shock tunnel. (See appendix A.)

Axial force.- The axial-force coefficients from the two sets of tests are presented in figure 4(b). This figure shows not only a wide variation of axial-force

coefficient with Reynolds number - as expected within a given facility - but a marked variation of axial-force coefficient between facilities at approximately the same Mach and Reynolds numbers. A discussion of the variation of the axial force between the two facilities at similar flow conditions must be based on theoretical considerations because the identical model was used for both sets of tests. There were two main differences between the blowdown-tunnel and shock-tunnel tests. First, the model wall temperatures were nearly 60 percent higher in the blowdown tunnel where the model was subjected to about 10 seconds of hot hypersonic flow 1135°R to 1480°R before data were recorded. The wall temperature of the model in the shock tunnel was at an ambient temperature of about 540°R before the run that lasted less than 0.015 second, thereby allowing the model walls little time to heat up. The estimated average model wall temperature for the LRC blowdown-tunnel tests was 860°R, or about 320°R higher than the known model wall temperature during the shock-tunnel tests. The second major difference between the tests was the much higher stagnation temperatures for the shock-tunnel tests, particularly at the low Reynolds number. The difference amounted to about 640°R at $R_l = 23.79 \times 10^6$ and 2240°R at $R_l = 1.69 \times 10^6$. The variation of model wall temperatures when combined with the widely different stagnation temperatures produces values of T_w/T_o, a highly significant boundary-layer parameter, as high as 0.64 for the blowdown-tunnel tests to as low as 0.16 for the shock-tunnel tests. Both laminar and turbulent boundary-layer theories are based on equations that have been derived in terms of the local Mach and Reynolds numbers and the ratio of wall temperature to stagnation temperature or the ratio of wall temperature to boundary-layer edge temperature; thus, variations of boundary-layer thickness and skin friction would be expected to exist between the two test facilities. The high stagnation temperatures of the Calspan tests combined with an approximate constant Mach number resulted in high stream static temperatures which, as discussed in the theoretical-methods section and appendix B, were responsible for skin-friction coefficients nearly equal to those of the LRC hot-wall tests made with low stream static temperatures. The cold-wall conditions of the model during the Calspan tests contributed to the laminar boundary-layer stability which will be discussed subsequently.

To facilitate a comparison between the data from the two tunnels, the same symbols were used for similar Reynolds numbers on the two parts of figure 4(b). Theoretical estimates were made assuming either all-laminar or predominantly all-turbulent skin friction. For consistency, therefore, only the lower and higher Reynolds number viscous estimates are presented, as the intermediate Reynolds number data are considered to contain a high percentage of transitional flow which cannot presently be predicted by the computer program. It may be seen that the experimental axial-force coefficients from the blowdown tunnel were consistently higher than those from the shock tunnel. This trend was predicted by Monaghan's laminar T'-theory, which as presented herein included skin friction, induced pressure, and viscous-interaction increments; but the turbulent Spalding-Chi theory predicted slightly lower estimates for the hot-wall blowdown-tunnel results. Predictions of the cold-wall shock-tunnel results by either laminar or turbulent theory were consistently superior to those for the blowdown tunnel at all Reynolds numbers. This was partly due to the lack of knowledge of the model-wall-temperature distribution during the blowdown-tunnel tests and to the larger induced pressure effects at the lower Reynolds numbers. These induced pressure effects were only partially taken into account by the computer program and will be discussed subsequently. The overall trend of the variations of axial force with angle of attack was accurately predicted by the GHABAP. It should be noted (fig. 4(b)) that the predicted increments of skin friction, taken as the difference between the leading-edge axial-force curves and the individual total axial-force curves (labeled "Turbulent C_F" and "Laminar C_F"), tend to increase with angle of attack. These increments of skin friction increase more

rapidly for the turbulent than for the laminar estimates, a trend that was accurately predicted by the GHABAP. The short curves at $\alpha = 3°$ labeled "With δ*Cal." are estimates made by the present methods and will be discussed subsequently.

Improvements of complex configuration axial-force prediction at hypersonic speeds depend on a better understanding of the model wall temperature distribution, a revision of computer programs to calculate pressure distributions and skin friction along surface streamlines in lieu of the present streamwise or longitudinal flow assumption, and advanced methods of accounting for the laminar induced pressure effects on local pressures and skin friction. Local areas of boundary-layer transition and/or separation must also be accounted for.

Lift.- The lift coefficients are shown in figure 4(c), along with theoretical predictions for the highest and lowest Reynolds number tests. It may be seen that there was little difference between the lift-coefficient data taken at different Reynolds numbers or between facilities. Predictions of lift coefficient are considered adequate for preliminary design, but the predicted slope of C_L with angle of attack is slightly high. This is due in part to the buildup of boundary layer which tends to effectively distort the model surfaces in such a way as to decrease the experimental lift-curve slope. This observation stems from two-dimensional shock-expansion calculations made on wings having wedge-slab-wedge airfoils similar to the present model wing airfoil and an airfoil designed from the boundary-layer profiles discussed in appendix B. These calculations showed that the normal-force coefficient was decreased and that the axial-force coefficient increased on the wing having the boundary-layer-shaped airfoil when compared with the wedge-slab-wedge airfoil. Both of these forces contribute to a decrease in the lift coefficient at a given angle of attack, which results in a decrease in the slope of the lift curve with angle of attack.

Drag.- Comparisons of the experimental drag coefficients and theoretical estimates are presented in figure 4(d) for the various test Reynolds numbers. Because the drag coefficients are determined from a combination of the normal- and axial-force coefficients and the predictions of the normal force were superior to those of axial force, the variations between the experimental drag and theory are primarily due to the errors in the prediction of axial force. Again, the shock-tunnel results are better predicted than the blowdown-tunnel results throughout the angle-of-attack range for all test Reynolds numbers.

Lift-drag ratio.- The lift-drag ratio versus the angle of attack is presented in figure 4(e), along with theoretical estimates. A maximum lift-drag ratio of just over 6 was measured on the present wing-body model at the highest average shock-tunnel Reynolds number of 156.22×10^6. A loss of about 0.5 in L/D was recorded with a reduction of R_l to 32.59×10^6 and 24.32×10^6 for the two test facilities. These results compare favorably with the $M = 6$ data of reference 13 on a similar but not identical body-wing model at a Reynolds number of about 21×10^6. Estimates by the present theoretical methods tend to overpredict the lift-drag ratios at all angles of attack for both laminar and turbulent conditions. This is again primarily due to the inaccurate axial-force predictions that, in turn, were due to a variety of reasons discussed previously, including the lack of knowledge of the model wall temperature distribution, the assumption within the computer program that the flow on the model is always streamwise for pressure calculations and longitudinal on the model with no cross flow for skin-friction estimates, and inadequate estimates of induced pressure effects. Also, local areas of transition and/or separation were not taken into account by the present computer program.

Drag due to lift.- The drag due to lift is presented in figure 4(f), accompanied by calculated estimates. Of interest is the more linear nature of the experimental data than the theoretical curves. With improved estimates of drag, particularly for the blowdown-wind-tunnel data, adequate estimates of drag due to lift may be expected at all Reynolds numbers and at angles of attack higher than that required for maximum lift-drag ratio. The slope with C_L^2 of the inviscid drag curves and the laminar total drag curves are almost the same while the turbulent drag curves have a slightly higher slope, a variation due to the change in axial-force increments as pointed out previously.

Longitudinal stability.- The longitudinal stability is presented in figure 4(g) for the various test Reynolds numbers and may be seen to be approximately neutral about the 6.15 percent $\bar{c}$ moment-reference station. The GHABAP gives reasonable estimates of the longitudinal stability, but the underestimation in the level of the pitching moments which occurred in four out of the six tests could lead to poor estimates of trim. To obtain positive stability, the center of gravity must be placed farther forward than the present moment-reference station of 6.15 percent $\bar{c}$, $0.566l$. (See fig. 1.) However, such a forward location of the center of gravity could produce an overly stable condition at high subsonic and low supersonic speeds that could require excessive control power. A redistribution of planform ahead of the wing, or a shift of the wing on the present body, could provide a more favorable compromise.

Comparison of Experiment and Theory at a Constant Angle of Attack

An extensive study was carried out at a constant angle of attack of 3° over the complete range of experimental Reynolds number to assess the improvement in aerodynamic efficiency with increasing Reynolds number and to gain an understanding of the deficiencies of the available theoretical prediction methods. The angle of 3° was selected for the wide-range study because the angle of attack of 3° was approximately the angle of attack for maximum lift-drag ratio at the highest test Reynolds number of 156.22×10^6 (see fig. 4(e)).

The normal-force coefficient is shown in figure 5 to be essentially independent of Reynolds number for both the hot-wall tests from the LRC wind tunnel and the cold-wall tests of reference 1 from the Calspan shock tunnel. This conclusion may be better understood if consideration is given as to what happens with variations of Reynolds number. The primary effect of decreasing Reynolds number is a rapid thickening of the boundary layer, particularly under laminar conditions. The thickness of the boundary layer is dependent on the Mach, Reynolds, and Prandtl numbers, the local gas and model-wall temperatures, and the viscosity and specific heat of the test gas which, for the present tests, was dry air. This boundary layer forms on the upper surfaces as well as the lower surfaces and, as discussed in appendix B, alters the surface pressures in a manner that always increases the axial force but minimizes the variations in normal force at low angles of attack by inducing positive pressures on the upper surface as well as on the lower surface. Excellent predictions of the normal-force coefficient on the wing-body configuration with Reynolds number by the GHABAP are shown.

In contrast to the nearly constant normal-force coefficient with Reynolds number, the axial-force coefficient may be seen to decrease as expected from theoretical considerations by more than 50 percent through the same Reynolds number range. Possibly of more importance is the difference between the axial forces measured in the

two facilities. There was about a 16-percent increase in the axial-force coefficients measured at low Reynolds numbers on the model mounted in the LRC wind tunnel compared to those measured on the same model mounted in the Calspan shock tunnel at about the same Mach number and Reynolds number. The major difference between the two tests was the average wall temperatures of the model and the test-gas temperatures, or more exactly the ratios of average wall temperature to stagnation temperature which were about 0.64 for the LRC tests and 0.16 for the Calspan tests. The average wall temperature of the LRC tests was estimated to be 860°R and the wall temperature of the model in the Calspan shock tunnel was measured at 540°R. The comparative noise levels between the facilities were unknown, but the test section of the Calspan tunnel was 30 percent larger than that of the LRC tunnel.

At lower Reynolds numbers up to $R_l = 3 \times 10^6$ where the boundary layer is predominantly laminar, the GHABAP theory underpredicts the experiment for both sets of tests, but particularly so for the hot-wall LRC wind-tunnel data. The laminar theory presented on figure 5 included the sum of inviscid estimates made by assuming tangent-wedge pressures on the wings including fuselage-carry-through and tangent-cone pressures on the low-aspect-ratio nose and strakes. Added to this were viscous estimates made by using the Monaghan T'-theory to calculate skin friction, plus induced pressure estimates and viscous interaction corrections utilizing hypersonic similarity theory of references 14 to 16, all calculated by the GHABAP. The leading- and trailing-edge drag estimates were calculated separately and added to obtain the total axial-force coefficient $C_{A,total}$. (See figs. 5 and 7.)

Predictions at Reynolds numbers above about 15×10^6 were only fair where an all-turbulent boundary layer was assumed and the Spalding and Chi turbulent skin-friction theory was used. This underprediction of the turbulent viscous effects was due in part to the lack of the addition of increments of drag due to either the boundary-layer induced pressures or the viscous interaction and the use of the nose and leading edge for the origin of the turbulent boundary layers by the GHABAP rather than the virtual-origin concepts of reference 17. The Reynolds number range from about 3×10^6 to 15×10^6 was a mixed flow region with a combination of laminar, transitional, and turbulent flow, the viscous aerodynamics of which could not be determined by the present GHABAP.

From these studies it may be concluded that the normal-force coefficient is essentially independent of Reynolds number and wall temperature and that the GHABAP predicts reasonably accurate normal-force coefficients over a wide Reynolds number range for the present class of configuration. The GHABAP predictions for axial-force coefficient leave much to be desired, and it was not clear whether the difference between experiment and theory was due to errors in the predicted inviscid axial force, the induced pressure correction, the estimated skin friction, or the viscous interaction correction. The next section presents a study of the experimental data to provide an insight into the prediction of the inviscid axial-force coefficient.

Estimation of Inviscid Pressure Forces by Extrapolation of Axial-Force Data to Very High Reynolds Numbers

The comparison of experimental axial-force coefficients with theoretical results made with the GHABAP showed that the best correlation existed at Reynolds numbers where the boundary layer was thinnest. Thin boundary layers are generally associated only with high Reynolds numbers; however, cold-wall temperatures produce a thinner boundary layer than do hot-wall temperatures. It was the low Reynolds number cold-wall tests and those at high Reynolds number turbulent conditions that showed the

best correlation with theory. A study was therefore undertaken to gain a better understanding of what might be expected with the present test configuration under very high Reynolds number conditions where the boundary layer would be very thin; the results are presented in figure 6.

It is well-known that laminar boundary-layer parameters including laminar skin friction are functions of the reciprocal of the square root of the Reynolds number. To obtain an estimate of the laminar Reynolds number test range, the axial-force coefficients for all $\alpha = 3°$ tests were plotted against $1/\sqrt{R_l}$ and are presented in figure 6(a). Lines were faired through the lower Reynolds number data and extrapolated as a straight line to $1/\sqrt{R_l} = 0$ or effectively to a very high Reynolds number. Only minimal compromise was required to make the fairings converge to the inviscid value of $C_A = 0.0022$ obtained from the GHABAP plus leading- and trailing-edge drag. From this set of data and faired curves it may be concluded that the GHABAP gives accurate predictions of axial-force coefficient at low angles of attack for this class of vehicle at very high Reynolds numbers or under inviscid conditions. The change in slope of the data from the faired curves gives an estimate of the Reynolds number where transition begins and where the turbulent boundary layer begins to dominate the model boundary-layer flow. It may be inferred from these faired data that the flow over the model was predominantly laminar at the lower Reynolds numbers and that the difference between the present laminar-theory predictions and the experimental axial-force data is a failure of the theory to correctly model the flow, not an error in the assumption of the existence of laminar flow conditions.

This relatively successful extrapolation of the low Reynolds number data to very high Reynolds numbers utilizing the assumptions of laminar flow theory suggested that a similar extrapolation effort be made for the turbulent Reynolds number range. A root of 1/5 was tried and found unsatisfactory. Therefore, to determine the root of the turbulent Reynolds number range of experimental data, a plot of the experimental axial-force coefficients minus the inviscid coefficient of 0.0022 was prepared. This plot, figure 6(b), was made on full logarithmic paper to best illustrate the variation of the approximate skin-friction coefficient or net axial-force coefficient with increasing Reynolds number. As was expected from the results of an examination of figure 6(a), the net skin-friction coefficient at low Reynolds numbers plotted not only as a straight line but as having a slope of 1:2 which corresponds to the laminar square root of the Reynolds number. A careful fairing of the data at the higher Reynolds numbers produced a slope of 1:7 (i.e., 1/7 root) which historically has been associated with turbulent boundary-layer parameters. Figure 6(c) shows the experimental data plotted against the parameter $1/\sqrt[7]{R_l}$; again, straight-line fairings of the data extrapolate to the inviscid value of axial-force coefficient of 0.0022 determined by the GHABAP. The abrupt change in slope of the data from the faired curves is more pronounced here in figures 6(b) and 6(c) than in figure 6(a), and transition appears to begin at about $R_l = 3.4 \times 10^6$ for the LRC wind-tunnel hot-wall data and about $R_l = 4.5 \times 10^6$ for the Calspan shock-tunnel cold-wall data. A study of figure 6(c) provides additional evidence that the experimental data taken at Reynolds numbers of about 10×10^6 to 15×10^6 and above are predominantly turbulent and may be used to extrapolate the axial-force coefficient to very high flight Reynolds numbers. It may be concluded that the present tests were made under predominantly laminar flow conditions at the lower Reynolds numbers and predominantly turbulent flow conditions at the higher Reynolds numbers and that the GHABAP provides an excellent estimate of the inviscid axial-force coefficient.

The higher apparent transition Reynolds number of the shock-tunnel data may well have been due to the increased boundary-layer stability on the cold-wall model and a likely lower tunnel noise level. Laminar boundary-layer stability is that flow

quality which resists the progression to transition, and hence the development of a turbulent boundary layer, and can be affected by the Mach number, the ratio of wall to local temperature, and the noise emanating from the tunnel-wall boundary layer. As the present tests in both facilities were conducted under nearly constant Mach number conditions, it must have been the cold-wall condition of both the test model and the shock-tunnel walls and the larger test-section size of the shock tunnel that contributed to the observed higher transition Reynolds number. Cold-wall model tests, where the model walls absorb heat from the air, are known to delay transition; and larger test sections have been shown to have lower noise levels than smaller test sections at similar Mach and Reynolds number conditions. (See ref. 18.) It may be concluded that the observed higher transition Reynolds number of the shock-tunnel data was due in part to the cold-wall condition of the model and to the larger tunnel test section.

The next section will discuss the results of a study to improve the estimates of induced pressure effects on the axial-force coefficients.

AXIAL-FORCE PREDICTION USING PRESENT METHOD OF INDUCED PRESSURE EVALUATION

As summarized in the section entitled "Theoretical Methods," the laminar axial-force coefficients may be considered as a combination of the inviscid pressure forces including the wing and body leading-edge pressure force, the wing trailing-edge base pressure, the skin friction, the induced pressure due to boundary-layer growth, the variation of the skin friction due to the induced pressures (termed "viscous interaction" herein), and an increment of induced pressure due to leading-edge bluntness. The present study utilized each of the above factors except the bluntness induced pressure increment to evaluate the total axial-force coefficient of the present test configuration.

The buildup of the calculated laminar axial-force coefficients at $\alpha = 3°$ for the Reynolds number range from about 0.7×10^6 to 10×10^6 based on model theoretical length is presented in figure 7(a) for both the hot-wall and cold-wall test conditions. The inviscid body axial force $\Delta C_{A_{B,Inv}}$ and the body and wing skin friction ΔC_{F_B} and ΔC_{F_W} make up the largest portion of the total coefficient, with the change in the body and wing viscous interaction $\Delta C_{A_{B,VI}}$ and $\Delta C_{A_{W,VI}}$ making the next largest contribution (particularly for the hot-wall tests). The inviscid wing forces and the body and wing induced pressure increments are relatively small compared to the viscous forces. The increment of axial force $\Delta C_{A_{W,LE\&TE}}$ included a small estimate of drag due to the blunt trailing edge, as well as the leading-edge bluntness drag.

A comparison between the total calculated axial-force coefficients and the experimental data is presented in figure 7(b), from which it can be seen that considerable improvement has been made over the GHABAP predictions presented in figure 5. The major improvement appears to have come from the estimated increment of the change in skin friction due to induced pressure, particularly for the hot-wall case.

A comparison of the resulting lift, drag, and lift-drag ratio calculations utilizing the improved axial-force estimates and the experimental data are shown in fig-

ure 8. For the known laminar flow region below Reynolds numbers of about 3×10^6, the lift-drag estimates were in error by no more than about 10 percent for the scattered data points. Future improvements in this combination of methods of axial-force prediction are possible by taking into account any variation in wall temperature on the model, by using shock-expansion pressure-distribution predictions for the boundary-layer induced pressures, by making induced pressure corrections due to leading-edge bluntness, and by taking these induced pressures into account when estimating skin friction.

The final computed estimates of axial-force coefficient, drag coefficient, and lift-drag ratio, which are presented on figures 7 and 8, have been added to figures 4(b), 4(d), 4(e), and 4(f) at $\alpha = 3°$ and are labeled "With δ*Cal." A marked incremental improvement of the estimates is shown on figure 4 for the $R_l = 1.68 \times 10^6$ and 1.53×10^6 hot- and cold-wall tests, but a somewhat poorer correlation is shown with the $R_l = 0.597 \times 10^6$ cold-wall test.

It may be concluded that detailed calculations of the effects of induced pressure, particularly the variations of the skin friction due to induced pressures or viscous interaction, are required for accurate configuration performance estimates at low Reynolds numbers when the boundary layer is predominantly laminar.

CONCLUSIONS

An analysis of experimental data for a hydrogen-fueled, blended wing-body hypersonic transport concept from a conventional blowdown wind tunnel and a shock tunnel at a Mach number of about 8 through a Reynolds number range (based on fuselage theoretical length) from 0.597×10^6 to about 156.22×10^6 leads to the following conclusions:

1. There was a minimal variation of normal-force coefficient with Reynolds number, or between test facilities, although wide variations of model surface temperatures and tunnel stagnation temperatures existed between the blowdown and shock tunnels.

2. The minimal variation of normal-force coefficient with Reynolds number is indicative of an immunity of normal force to the effects of viscous boundary-layer variations due to changes in the ratio of wall temperature to stream temperature.

3. Good theoretical predictions of normal-force coefficient with angle of attack and with Reynolds number were made with the Mark III Gentry Hypersonic Arbitrary-Body Aerodynamics Program, particularly at possible cruise angles of attack, i.e., 2° to 5°.

4. Very high Reynolds number axial-force coefficients, approximating the inviscid values, may be estimated with the logarithmic extrapolation method presented.

5. The Mark III Gentry Hypersonic Arbitrary-Body Aerodynamics Program provides excellent estimates of the inviscid axial-force coefficients for the present blended wing-body configuration.

6. The low Reynolds number experimental tests were made under predominantly laminar flow conditions, and the high Reynolds number tests were made under predominantly turbulent flow conditions.

7. Higher transition Reynolds numbers occurred in the shock tunnel and were due to greater boundary-layer stability on the cold-wall model and the apparent lower noise level in the larger test section.

8. For a given hypersonic Mach number, the laminar skin friction decreased with increases in the ratio of wall temperature to local temperature or in stream static temperature or in both.

9. Satisfactory estimates of laminar axial-force coefficients, and thus configuration performance coefficients, can be made only when the effects of induced pressures have been taken into account, particularly the variations in skin friction due to induced pressure. Knowledge of wall temperature distributions, accounting for local areas of boundary-layer transition, and the calculation of pressure distributions and skin friction along surface streamlines would further improve calculations.

10. Estimates of turbulent axial-force coefficients and performance were only fair, due in part to the need of drag increments from boundary-layer induced pressures and viscous interaction and a computer program that uses the virtual-origin concept for the initiation of the turbulent boundary layers.

Langley Research Center
National Aeronautics and Space Administration
Hampton, VA 23665
May 4, 1983

APPENDIX A

HYPERSONIC TUNNEL CALIBRATION

Langley Mach 8 Variable-Density Tunnel

The circular cross-section axially symmetric nozzle design of the Langley Mach 8 Variable-Density Tunnel and the rapid expansion of the wall contour downstream from the first minimum contribute to a region of varying dynamic pressure near the longitudinal centerline of the test section. This focusing effect produces spikes in the calibration amounting to as much as +1.24 percent to -3.2 percent, of the average stream dynamic pressure over a region about 2 inches in diameter. (See fig. 9 taken from ref. 19.) The present tests were designed to have the model remain between this central core and the thick 3.5-inch tunnel-wall boundary layer.

Figure 10(a) shows a frontal view of the model at $\alpha \approx 0°$, 3°, and 6° mounted inverted in a region of undisturbed flow with the center of rotation at 2 inches below the tunnel centerline. The calibration of this nozzle consisted of a vertical and horizontal centerline survey at various longitudinal intervals through the test section at various stagnation pressures. A study of these data showed that the longitudinal average of measurements on the horizontal survey were approximately the same as average measurements on the vertical survey if they were made at the same radial distance from the nozzle centerline. This made it possible to estimate with confidence the Mach number on concentric contours about the nozzle centerline. These lines of constant average Mach number are shown in figure 10(b) superimposed on the frontal view of the model test region. The region shown was numerically integrated to obtain an overall average test Mach number for the various calibration stagnation-pressure levels. The results of this integration plotted as a straight line against stagnation pressure on semilogarithmic paper are presented in figure 11. The Reynolds number based on theoretical fuselage length (with boattail) and the average Mach number shown in this figure are also plotted as a straight line against stagnation pressure, but on full logarithmic paper.

Calspan 96-Inch Hypersonic Shock Tunnel

The authors were not involved in the calibration of the Calspan 96-Inch Hypersonic Shock Tunnel; this section is therefore limited to a description of the flow conditions for the tests reported in reference 1 and analyzed herein. As expected, the stagnation pressure was increased with required Reynolds number as presented in figure 12, but contrary to normal practice in a blowdown or continuous hypersonic tunnel, the stagnation temperature was increased at the lower Reynolds numbers to facilitate the production of low Reynolds number conditions by increasing the viscosity and decreasing the mass density. At the higher Reynolds number the total temperature was reduced to values just high enough to avoid air liquefaction, thereby minimizing the viscosity and maximizing the density to produce the nearly flight level Reynolds numbers. The variation of Mach number with Reynolds number (fig. 12) was somewhat less than that of the Langley Mach 8 Variable-Density Tunnel, had it been capable of being run at pressures sufficiently low and high enough to produce the same wide Reynolds number range. This was due to the use of interchangeable throats for the contoured nozzle which had an exit diameter of 24 inches.

APPENDIX B

LAMINAR SKIN FRICTION AND DISPLACEMENT BOUNDARY-LAYER THICKNESS

Laminar Skin Friction

The Gentry Hypersonic Arbitrary-Body Aerodynamics Program (GHABAP) utilizes Monaghan's T'-theory, or reference temperature method, of reference 8 for the calculation of laminar skin friction. This method is a semiempirical modification of the classic Blasius incompressible laminar skin friction by making the calculations on the flow properties based on a reference temperature rather than either the local stream or wall temperatures. For a flat plate the equation for local skin friction is

$$C_f\sqrt{R_{x,1}} = 0.664\sqrt{C} \tag{B1}$$

where

$$\sqrt{C} = \sqrt{\frac{T_1\mu'}{T'\mu_1}} \tag{B2}$$

and

$$T' = \frac{T_w}{T_1} - 0.468(N_{Pr})^{1/3}\left(\frac{T_w}{T_1} - \frac{T_{aw}}{T_1}\right) - 0.273N_{Pr}\left(\frac{\gamma - 1}{2}\right)M_1^2 \tag{B3}$$

since

$$\frac{T_{aw}}{T'} = 1 + (N_{Pr})^{1/2}\left(\frac{\gamma - 1}{2}\right)M_1^2 \tag{B4}$$

and

$$\frac{T_o}{T_1} = 1 + \left(\frac{\gamma - 1}{2}\right)M_1^2 \tag{B5}$$

equations (B3), (B4), and (B5) may be combined such that

$$\frac{T'}{T_1} = \frac{T_w}{T_1} + 0.468(N_{Pr})^{1/3}\left[1 - \frac{T_w}{T_1} + (N_{Pr})^{1/2}\frac{T_o}{T_1} - (N_{Pr})^{1/2}\right]$$

$$- 0.273N_{Pr}\frac{T_o}{T_1} + 0.273N_{Pr} \tag{B6}$$

With the substitution of Prandtl number, equation (B6) yields the following reference temperatures. For $N_{Pr} = 0.68$,

$$T' = 0.588T_w + 0.154T_o + 0.258T_1 \tag{B7}$$

for $N_{Pr} = 0.75$,

$$T' = 0.575T_w + 0.164T_o + 0.262T_1 \tag{B8}$$

and for $N_{Pr} = 1.0$,

$$T' = 0.532T_w + 0.195T_o + 0.273T_1 \tag{B9}$$

The similarity of these equations shows the relative insensitivity of the reference temperature to Prandtl number and thus a similar insensitivity of the calculated skin-friction coefficient to Prandtl number.

Plots of the laminar flat-plate skin-friction parameter $C_f\sqrt{R_{x,1}}$ from equation (B1) are presented in figure 13. Figure 13(a) shows the skin-friction parameter versus Mach number for a typical blowdown wind-tunnel stream static temperature of 100°R for various wall temperature ratios. This is the typical plot that is used to present hypersonic laminar skin friction; it shows a relative insensitivity of skin friction to Mach number but a considerable sensitivity to the wall temperature. From this plot it could be concluded that the laminar skin friction decreases with increased wall temperature; this is correct for a given stream static temperature. Because the present study concerns experimental data measured in two distinctly different temperature environments at approximately the same Mach number, figure 13(b) was generated at a constant Mach number of 8 with stream static temperature as the variable. Data points are included at the appropriate wall temperature ratios and stream static temperatures for the present Langley and the Calspan test conditions. It may be seen that the skin-friction parameter is slightly smaller for the cold-wall test condition because of the twofold to threefold increase in stream static temperature and the nearly 80 percent lower wall temperature ratio. It, therefore, may be concluded that for a constant Mach number the laminar skin friction decreases not only with increasing wall temperature but also with increasing stream static temperature.

Displacement Boundary-Layer Thickness

The reference temperature method of reference 8 was also used to study the induced pressure effects of boundary-layer buildup on the wing surfaces. An example of the large change in the measured surface pressures that may be expected near the leading edge of a wing in hypersonic flow and the resulting large favorable chordwise pressure gradient was first shown by Becker in reference 20. These experiments were made in the first hypersonic wind tunnel, the NACA/NASA Langley 11-Inch Hypersonic Tunnel, at a Mach number of 6.9. Wing surface pressures were accurately predicted using the contour of the displacement boundary-layer thickness as the effective wing surface.

APPENDIX B

Monaghan's equation for displacement thickness was derived in terms of free-stream Mach number, local unit Reynolds number, local and wall temperature, Prandtl number, and the Chapman-Rubesin viscosity-temperature relation. After terms are collected, Monaghan's equation can be written as follows:

$$\delta^*\sqrt{\frac{R_{unit}}{CX}} = \frac{2}{0.664}\left\{\frac{T_w}{T_1}\left[\frac{\pi}{2} - (N_{Pr})^{1/3}\right] + \left(\frac{\gamma - 1}{2} M_1^2\right)\left[(N_{Pr})^{5/6} - \frac{\pi N_{Pr}}{4}\right] + (N_{Pr})^{1/3} - 1\right\} \tag{B10}$$

With the substitutions of Prandtl number, equation (B10) simplifies to the following equations. For $N_{Pr} = 0.68$,

$$\delta^*\sqrt{\frac{R_{unit}}{CX}} = 2.083 \frac{T_w}{T_1} + 0.288(\gamma - 1)M_1^2 - 0.363 \tag{B11}$$

For $N_{Pr} = 0.75$,

$$\delta^*\sqrt{\frac{R_{unit}}{CX}} = 1.995 \frac{T_w}{T_1} + 0.298(\gamma - 1)M_1^2 - 0.275 \tag{B12}$$

For $N_{Pr} = 1.0$,

$$\delta^*\sqrt{\frac{R_{unit}}{CX}} = 1.719 \frac{T_w}{T_1} + 0.323(\gamma - 1)M_1^2 \tag{B13}$$

It may be noted that for $M_1 = 0$ and $T_w/T_1 = 1.0$ each equation reduces to approximately the classic equation of Blasius for low speeds, i.e.,

$$\delta^* = \frac{1.73X}{\sqrt{R_x}} \tag{B14}$$

Plots of the three equations (eqs. (B11) to (B13)) for $N_{Pr} = 0.68$, 0.75, and 1.0 are presented in figure 14 for local Mach numbers up to 10 and the ratios T_w/T_1 up to 16. To examine more closely the effect of Prandtl number on δ^*, a cross plot of $\delta^*\sqrt{R_{unit}/CX}$ versus T_w/T_1 is presented in figure 15 for a Mach number of 8. It may be seen that smaller values of $\delta^*\sqrt{R_{unit}/CX}$ are predicted for $N_{Pr} = 1.0$. To determine the difference between the prediction of δ^* by this method and by the more rigorous method of reference 10, figure 16 was generated for a laminar boundary layer at $M_1 = 8$ and a constant low Reynolds number of 0.384×10^6. For the range of wall-temperature ratios considered, it may be seen that the variation between the two dissimilar methods was no more than 5 percent for cold-wall test

conditions and about 3.5 percent for the hot-wall test condition. It was therefore concluded that the T'-theory of reference 8 was adequate for the present calculation procedure and the use of $N_{Pr} = 0.68$ would be the more realistic.

Equation (B11) may be written for $\gamma = 1.4$ as follows:

$$\delta^* = \frac{\sqrt{C}\sqrt{X}}{\sqrt{R_{unit}}}\left(2.083\,\frac{T_w}{T_1} + 0.1152M_1^{\,2} - 0.363\right) \tag{B15}$$

and

$$\frac{d\delta^*}{dX} = \frac{\sqrt{C}}{\sqrt{R_{unit}}}\,\frac{1}{2\sqrt{X}}\left(2.083\,\frac{T_w}{T_1} + 0.1152M_1^{\,2} - 0.363\right) \tag{B16}$$

which is the local slope, i.e., $\tan^{-1}$ of the angle between the wing surface and the curved boundary of the displacement thickness contour at station X. Combining equations (B15) and (B16) results in

$$\frac{d\delta^*}{dX} = \frac{\frac{d\delta^*}{dX}}{\delta^*}\,\delta^* = \frac{\frac{\sqrt{C}}{2\sqrt{R_{unit}}\sqrt{X}}}{\frac{\sqrt{C}\sqrt{X}}{\sqrt{R_{unit}}}}\,\delta^* = \frac{\frac{\delta^*}{2\sqrt{X}}}{\sqrt{X}} = \frac{\delta^*}{2X} \tag{B17}$$

which provides the following simple relation between the local slope of the contour of the displacement boundary layer and its thickness or depth:

$$\frac{d\delta^*}{dX} = \frac{\delta^*}{2X} \tag{B18}$$

Equations (B15) and (B18) were used extensively as discussed under the section entitled "Theoretical Methods."

Examples of the distribution of the displacement boundary layer are shown in figure 17 for the exposed wing root chord sections for both the hot- and cold-wall tests. These boundary-layer displacement thickness distributions were calculated by use of equation (B15) at a Mach number of 7.74 and a Reynolds number of 1.367×10^6 based on theoretical body length. The boundary layer is nearly twice as thick on the wing section from the hot-wall test than that from the cold-wall test; therefore, creating higher flow deflections just downstream of the leading edge, and thus higher induced pressures than were created during the cold-wall tests. Figure 18 illustrates the rapid variation of the slope of the displacement boundary layer which may be seen to decrease by about 95 percent in the first 10 percent of the wing root chord. An inset plot on figure 18 illustrates the variation of the tangent-wedge pressure ratio with the boundary-layer slope and the resulting flow deflection.

Although the forward surface of the boundary layer is blunt and may create a small region of detached flow and very high local pressures, the integrated pressure force is of little consequence due to the very small areas involved.

A typical calculated pressure distribution is presented in figure 19(a) for the exposed wing root chord of the model during the hot-wall test and for the variation of the integrated chordwise axial pressure distributions plotted with respect to the exposed wing semispan in figure 19(b). This figure illustrates the high calculated pressures at the leading edge on both the top and bottom wing surface for $\alpha = 3°$, which contributes substantially to the axial force but negligibly to the normal force due to the similar upper and lower surface pressure changes. The axial pressure coefficient is shown to increase spanwise and is a planform effect of wing taper due to the lower local Reynolds number at the tip and the resulting increased induced pressures.

APPENDIX C

EFFECT OF MODEL LOCATION AND TEST TIME ON FORCE-BALANCE DATA RECORDED IN LANGLEY MACH 8 VARIABLE-DENSITY TUNNEL

In general, hypersonic blowdown tunnels with axisymmetric nozzles have central test cores of nonuniform flow compared to the average test-section calibrated Mach number, as discussed in appendix A. In addition, hypersonic tunnels designed for about $M = 4$ and higher that operate at pressures above 400 psia require additional heat to be added to the air to prevent air condensation (liquefaction) during the expansion to test Mach number. This heated air often distorts the contoured tunnel walls, particularly in the vicinity of the nozzle throat or first minimum, resulting in a variation with time of the average test-section Mach number and the stream dynamic pressure.

The Langley Mach 8 Variable-Density Tunnel is a blowdown facility, has an axially symmetric nozzle, and utilizes high temperatures to test at high Mach numbers and thus meets all of the above criteria. A specific test was designed to determine the magnitude of the variations of these test conditions. It consisted of a series of tests at a constant angle of attack of 3° in which the model position was varied from 1 inch above the test section centerline to 2 inches below the centerline (fig. 20). The results of these tests are presented in figure 21 and show that the lift coefficient varied up to as much as 6 percent at the lower Reynolds number and that the pitching moment varied more than 20 percent at the intermediate and higher Reynolds numbers. It was therefore concluded that all other tests would be conducted with the model in the more uniform air 2 inches below the centerline.

During the position tests, data were taken at approximately 5-second intervals, and the results are presented in figure 22 using expanded scales. It may be seen that there was a variation of coefficient with time at all model positions and that the lift coefficient decreased and the pitching-moment coefficient increased. Part of these variations was due to the heating up of the model nonuniformly and thereby contributing to variation in heat load to the water-cooled shield of the balance and possibly unsymmetrical heating of the strain gages. It was, therefore, decided to utilize where possible only those data recorded at about 10 seconds for analysis and inclusion in the present report.

REFERENCES

1. Penland, J. A.; and Romeo, D. J.: Advances in Hypersonic Exploration Capability - Wind Tunnel to Flight Reynolds Number. J. Aircr., vol. 8, no. 11, Nov. 1971, pp. 881-884.

2. Gentry, Arvel E.: Hypersonic Arbitrary-Body Aerodynamic Computer Program (Mark III Version). Vol. I - User's Manual. Rep. DAC 61552, Vol. I (Air Force Contract Nos. F33615 67 C 1008 and F33615 67 C 1602), McDonnell Douglas Corp., Apr. 1968. (Available from DTIC as AD 851 811.)

3. Sears, William R.: On Projectiles of Minimum Wave Drag. Q. Appl. Math., vol. IV, no. 4, Jan. 1947, pp. 361-366.

4. Daum, Fred L.; and Gyarmathy, George: Condensation of Air and Nitrogen in Hypersonic Wind Tunnels. AIAA J., vol. 6, no. 3, Mar. 1968, pp. 458-465.

5. Hypersonic Shock Tunnel - Description and Capabilities. Calspan Corp., Sept. 1975.

6. Penland, Jim A.: Aerodynamic Characteristics of a Circular Cylinder at Mach Number 6.86 and Angles of Attack up to 90°. NACA TN 3861, 1957. (Supersedes NACA RM L54A14.)

7. Mayer, John P.: A Limit Pressure Coefficient and an Estimation of Limit Forces on Airfoils at Supersonic Speeds. NACA RM L8F23, 1948.

8. Monaghan, R. J.: An Approximate Solution of the Compressible Laminar Boundary Layer on a Flat Plate. R. & M. 2760, British A.R.C., 1953.

9. Spalding, D. B.; and Chi, S. W.: The Drag of a Compressible Turbulent Boundary Layer on a Smooth Flat Plate With and Without Heat Transfer. J. Fluid Mech., vol. 18, pt. 1, Jan. 1964, pp. 117-143.

10. Price, Joseph M.; and Harris, Julius E.: Computer Program for Solving Compressible Nonsimilar-Boundary-Layer Equations for Laminar, Transitional, or Turbulent Flows of a Perfect Gas. NASA TM X-2458, 1972.

11. Bertram, Mitchel H.; and Feller, William V.: A Simple Method for Determining Heat Transfer, Skin Friction, and Boundary-Layer Thickness for Hypersonic Laminar Boundary-Layer Flows in a Pressure Gradient. NASA MEMO 5-24-59L, 1959.

12. Bertram, Mitchel H.: Viscous and Leading-Edge Thickness Effects on the Pressures on the Surface of a Flat Plate in Hypersonic Flow. J. Aeronaut. Sci., vol. 21, no. 6, June 1954, pp. 430-431.

13. Ellison, James C.: Investigation of the Aerodynamic Characteristics of a Hypersonic Transport Model at Mach Numbers to 6. NASA TN D-6191, 1971.

14. Bertram, Mitchel H.; and Blackstock, Thomas A.: Some Simple Solutions to the Problem of Predicting Boundary-Layer Self-Induced Pressures. NASA TN D-798, 1961.

15. White, Frank M., Jr.: Hypersonic Laminar Viscous Interactions on Inclined Flat Plates. ARS J., vol. 32, no. 5, May 1962, pp. 780-781.

16. Bertram, Mitchel H.: Hypersonic Laminar Viscous Interaction Effects on the Aerodynamics of Two-Dimensional Wedge and Triangular Planform Wings. NASA TN D-3523, 1966.

17. Cary, Aubrey M., Jr.; and Bertram, Mitchel H.: Engineering Prediction of Turbulent Skin Friction and Heat Transfer in High-Speed Flow. NASA TN D-7507, 1974.

18. Pate, Samuel R.: Effects of Wind Tunnel Disturbances on Boundary-Layer Transition With Emphasis on Radiated Noise: A Review. AIAA-80-0431, Mar. 1980.

19. Goldberg, Theodore J.; Hefner, Jerry N.; and Stone, David R.: Hypersonic Aerodynamic Characteristics of Two Delta-Wing X-15 Airplane Configurations. NASA TN D-5498, 1969.

20. Becker, John V.: Results of Recent Hypersonic and Unsteady Flow Research at the Langley Aeronautical Laboratory. J. Appl. Phys., vol. 21, no. 7, July 1950, pp. 619-628.

TABLE I.- GEOMETRIC CHARACTERISTICS OF MODEL

Wing:	
Reference area (includes area projected to fuselage centerline), cm^2 (in^2)	451.64 (70.00)
Exposed area outboard of strakes, cm^2 (in^2)	195.04 (30.23)
Wetted area, cm^2 (in^2)	390.09 (60.42)
Span, cm (in.)	24.71 (9.730)
Aspect ratio	1.353
Root chord (on fuselage centerline), cm (in.)	33.24 (13.086)
Tip chord, cm (in.)	3.32 (1.308)
Taper ratio	0.099
Mean aerodynamic chord, cm (in.)	22.38 (8.810)
Sweepback angle, deg:	
Leading edge	65.0
25-percent chord line	56.99
Trailing edge	-15.4
Dihedral angle (airfoil mean line), deg	0
Incidence angle, deg	0
Wing airfoil section (see fig. 1):	
Thickness ratio of -	
Exposed root	0.03
Tip	0.03
Leading-edge radius, cm (in.):	
Fuselage centerline chord	0.00762 (0.003)
Tip	0.00762 (0.003)
Trailing-edge height	0.01524 (0.006)
Center fin proposed (vertical tail):	
Area (exposed), cm^2 (in^2)	79.99 (12.399)
Span (exposed), cm (in.)	9.33 (3.672)
Aspect ratio of exposed area	1.09
Root chord (fuselage surface line), cm (in.)	13.59 (5.353)
Tip chord, cm (in.)	3.53 (1.390)
Taper ratio	0.259
Mean aerodynamic chord of exposed area, cm (in.)	9.55 (3.759)
Sweepback angle, deg:	
Leading edge	60
Trailing edge	-30
Fin airfoil section, variable:	
Thickness ratio of -	
Tip trailing edge	0.06
Root trailing edge	0.06
Leading-edge radius, cm (in.)	0.003
Fuselage:	
Length, cm (in.) theoretical model	65.84 (25.92)
Length, cm (in.) test model	59.95 (23.61)
Maximum height, cm (in.)	3.63 (1.428)
Maximum width excluding strakes, cm (in.)	7.25 (2.856)
Nose radius, cm (in.)	0.00762 (0.003)
Fineness ratio of equivalent round body (excluding strakes)	13.0
Base area, cm^2 (in^2)	11.03 (1.710)
Complete model (excluding vertical tail and engine):	
Planform area of theoretical model, cm^2 (in^2)	648.69 (100.541)
Planform area of test model, cm^2 (in^2)	633.38 (98.268)
Aspect ratio of theoretical-model planform	0.942
Aspect ratio of test-model planform	0.963
Wetted area, approximate, cm^2 (in^2)	1451.70 (225.0)
Model scramjet engine (proposed):	
Frontal area, 2 percent wing area, cm^2 (in^2)	9.03 (1.40)
Chord ratio of width to height	4.8
Volume of test model, cm (in^3)	896.46 (54.70)
$V^{2/3}/A_p$ (test model)	0.146

TABLE II.- CROSS-SECTIONAL DIMENSIONS OF FUSELAGE

[All values are in inches]

X/l	X	H	A	rad. B	rad. T	rad. US	rad. LS	rad. E	Sd	SW	rad. W
0	0	0	0.396	0	0	0	0	0	0	0	
.067	1.728	.411	.194	1.508	.465	.084	.632	.103	.101	.084	
.133	3.456	.663	.083	2.436	.752	.389	1.264	.166	.163	.154	
.200	5.184	.862	.025	3.164	.977	.457	1.897	.216	.212	.216	
.267	6.912	1.022	0	3.751	1.158	.533	2.529	.255	.251	.274	
.333	8.639	1.151	0	4.233	1.304	.547	3.161	.288	.283	.332	
.400	10.368	1.253	0	4.597	1.419	.590	3.791	.313	.308	.383	
.467	12.096	1.316	0	4.828	1.491	.644	4.424	.329	.324	.429	
.533	13.824	1.379	0	5.058	1.562	.634	5.058	.345	.339	.465	
.600	15.552	1.426	0	5.234	1.616	*.522	5.234	.357	.353	†1.014	1.440
.667	17.279	1.428	0	5.242	1.618	*.392		.357	.351	†1.819	3.870
.700	18.144	1.426	0	5.234	1.616	*.389		.356	.342	†2.224	4.320
.733	19.008	1.378	.007	5.058	1.562	*.432		.345	.313	†2.676	1.800
.767	19.872	1.316	.032	4.828	1.491	*.457		.329	.281	†3.141	1.080
.800	20.736	1.253	.076	4.597	1.419	*.529		.313	.245	†3.607	1.800
.833	21.599	1.151	.126	4.223	1.304	*.601		.288	.198	†3.174	2.016
.867	22.464	1.022	.180	3.751	1.158	0		.256	.117	2.485	2.808
.900	23.328	.862	.230	3.164	.977			.216			
.933	24.192	.663	.284	2.436	.752			.166			
.967	25.056	.411	.338	1.508	.465			.103			
1.000	25.920	0	.396	0	0			0			

*Fairing to wing.
†Distance to leading edge or tip.

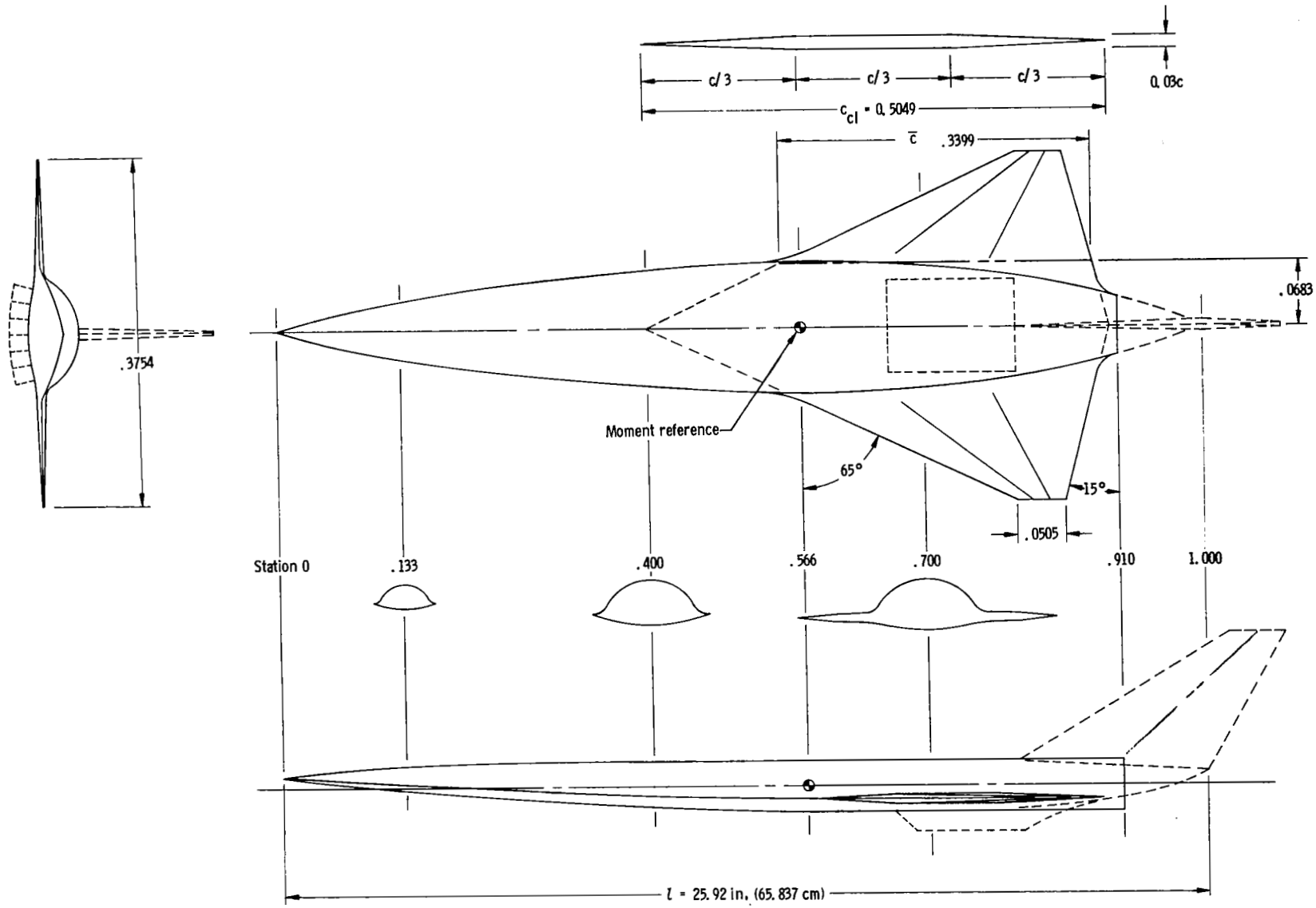

Figure 1.- Details of wind-tunnel model. All dimensions have been normalized by the fuselage theoretical length ℓ = 25.92 in. Dashed lines show components not used in present test.

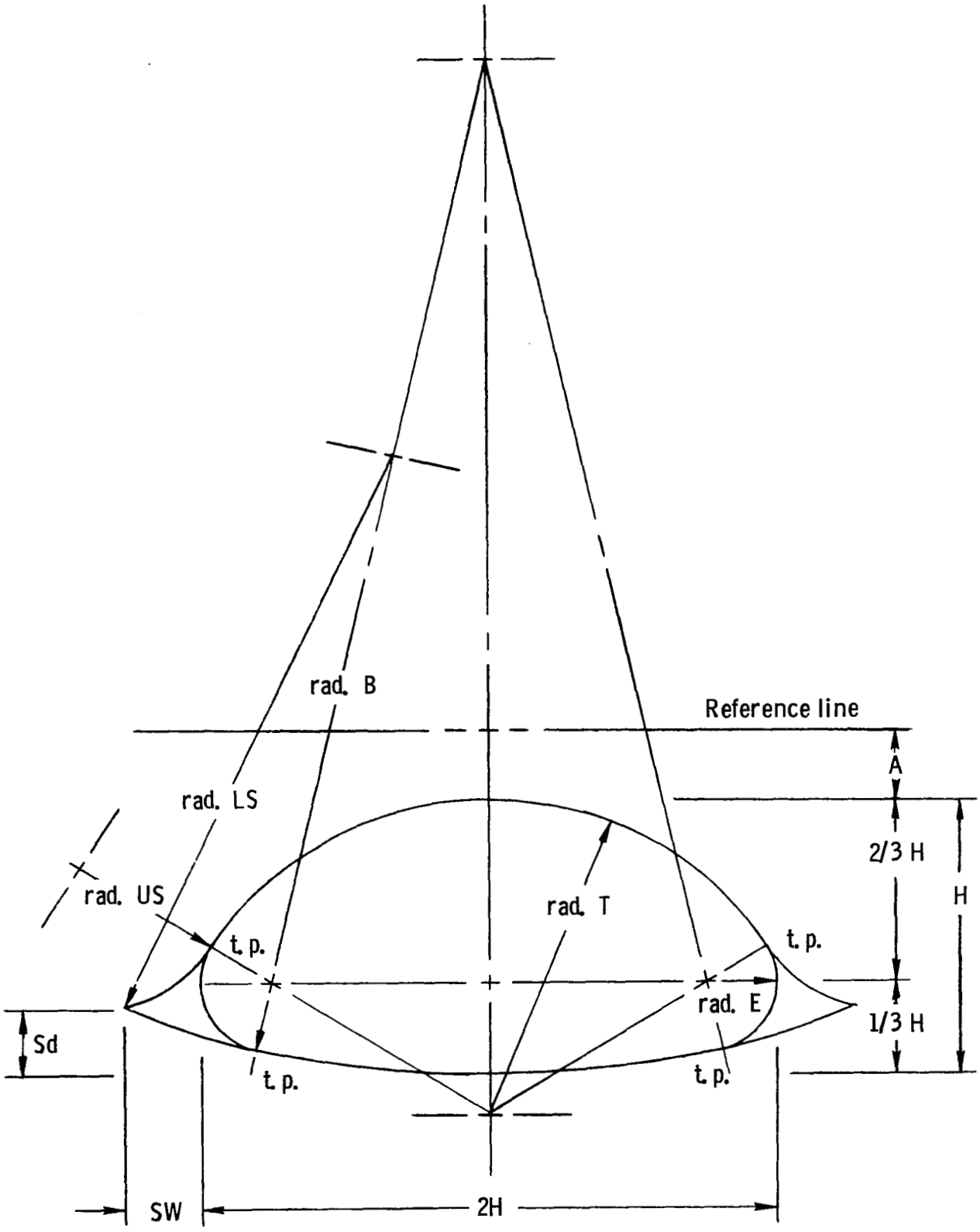

Figure 2.- Detail of fuselage cross section and strake design. Dimensions are listed in table II.

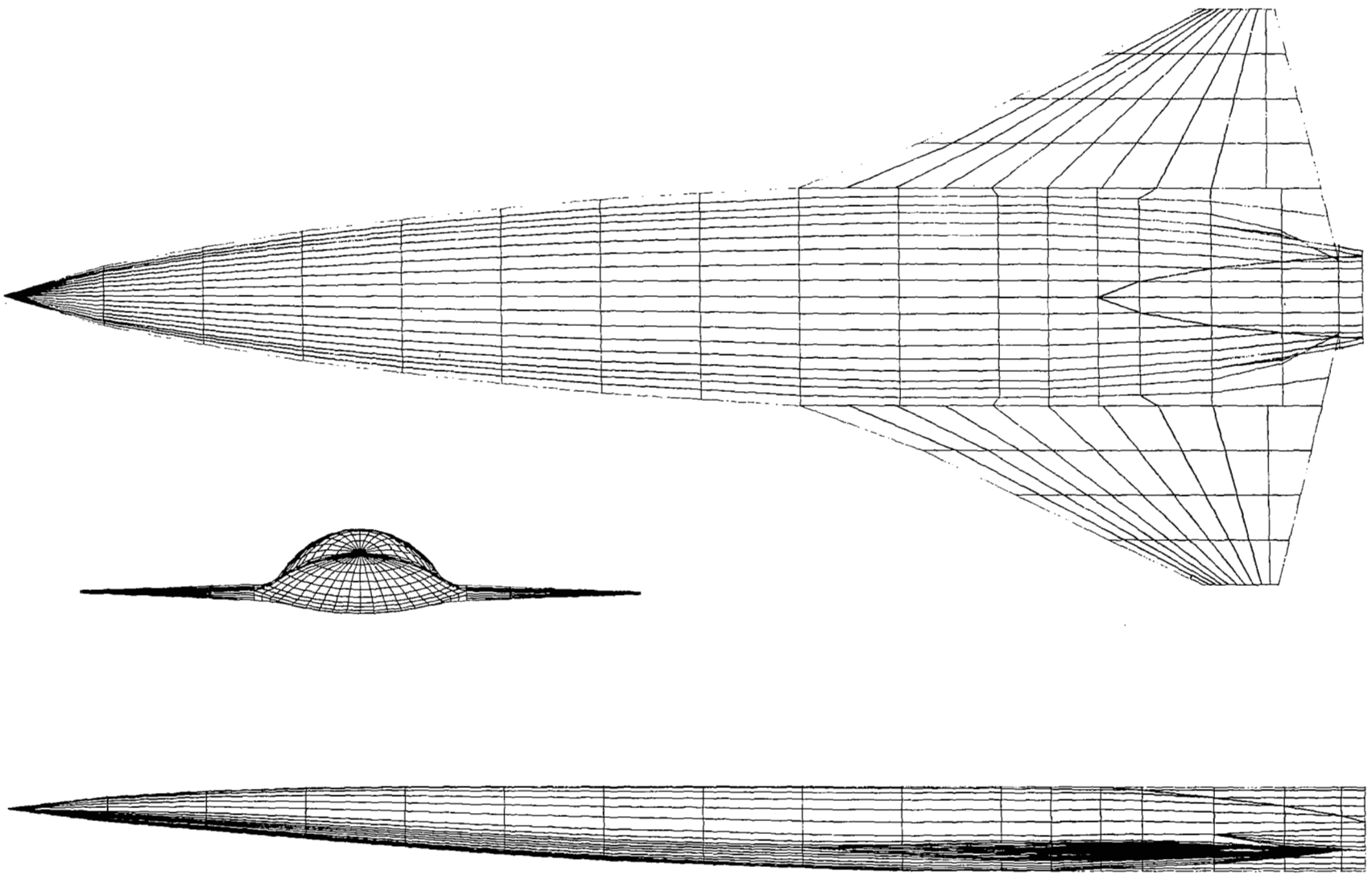

Figure 3.- Computer drawing of paneling scheme of configuration as input for hypersonic aerodynamic calculations.

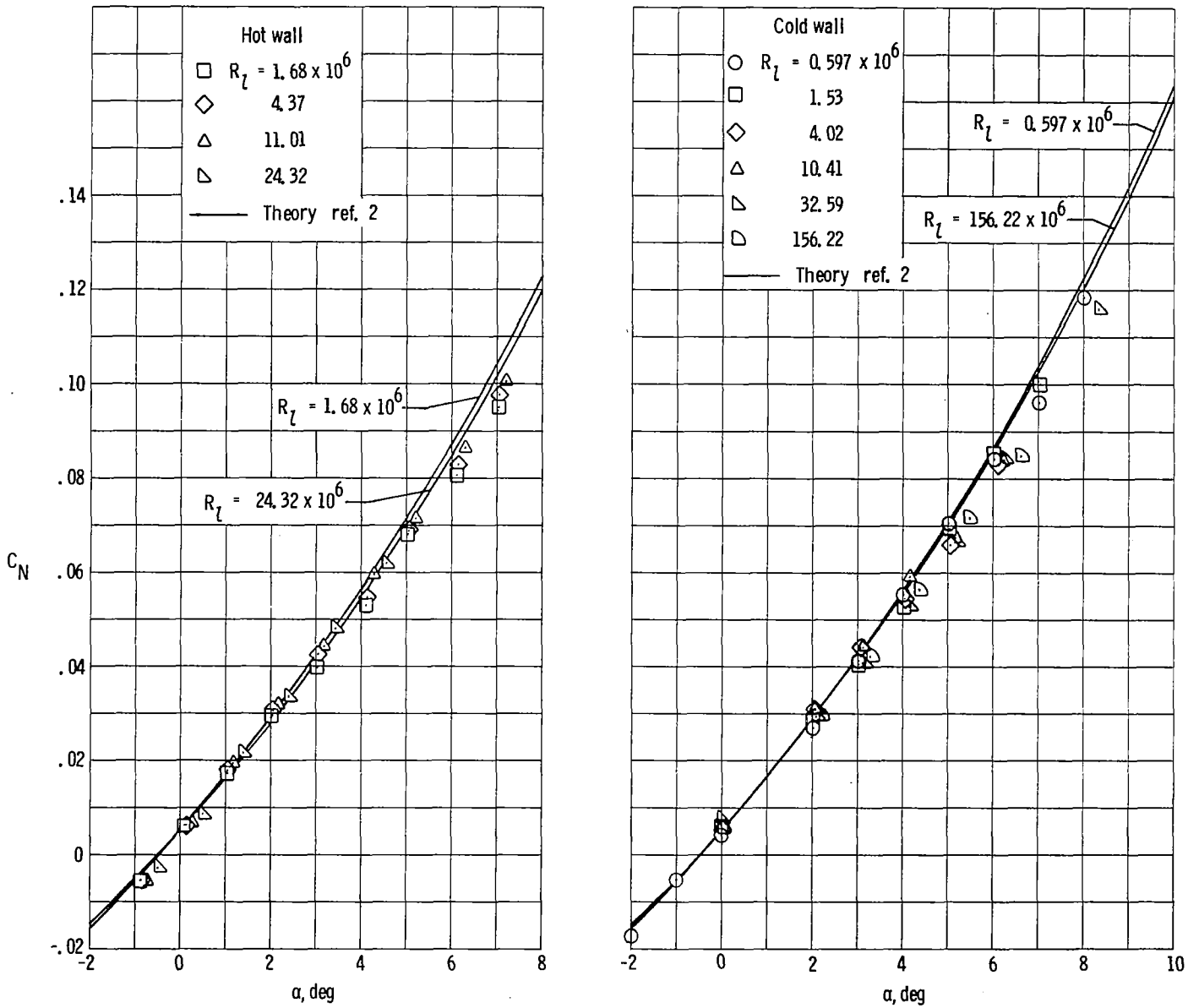

(a) Normal force.

Figure 4.- Comparison of theoretical force and moment coefficients with experimental data for various Reynolds numbers in the Langley Mach 8 Variable-Density Tunnel and the Calspan 96-Inch Hypersonic Shock Tunnel.

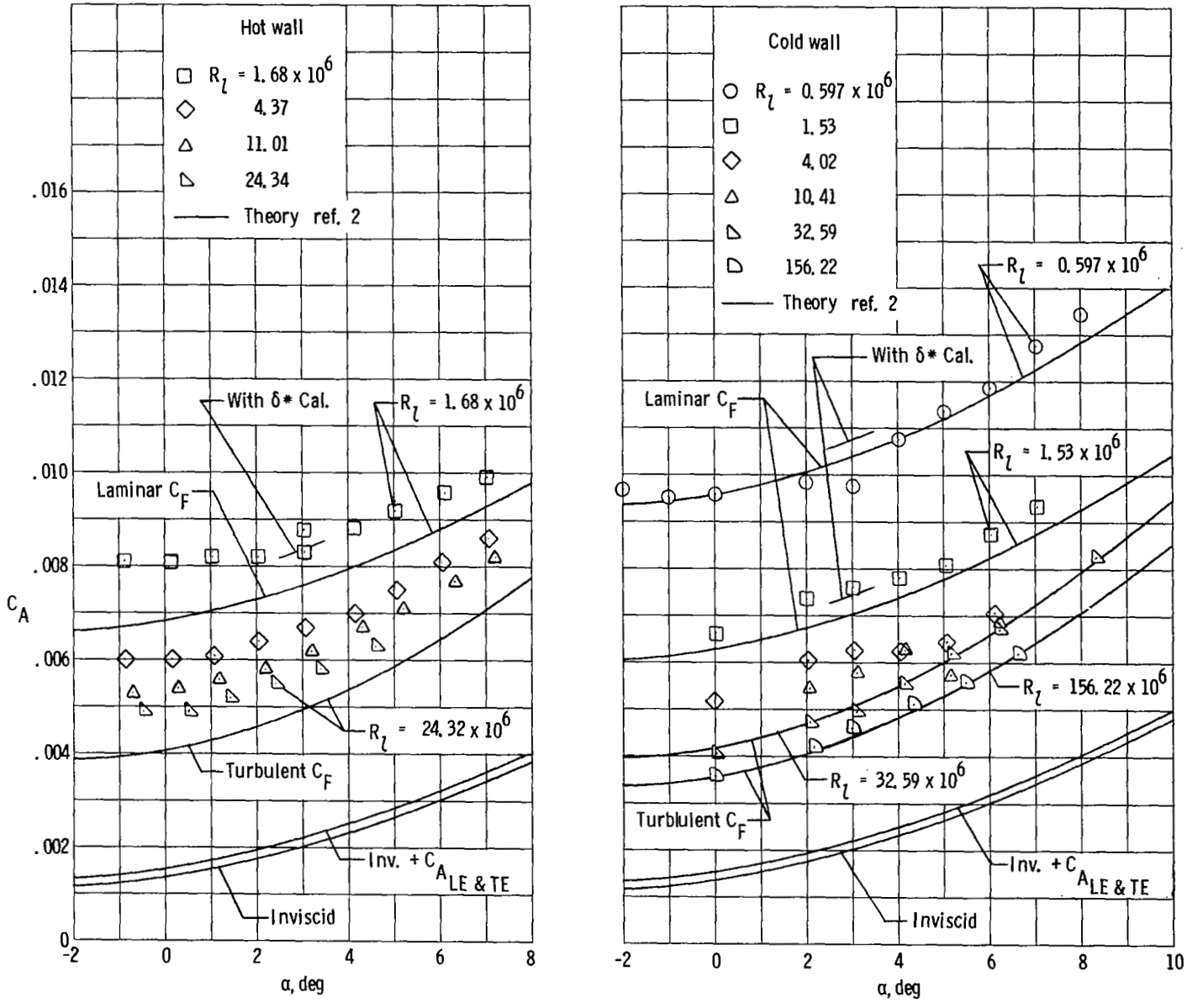

(b) Axial force.

Figure 4.- Continued.

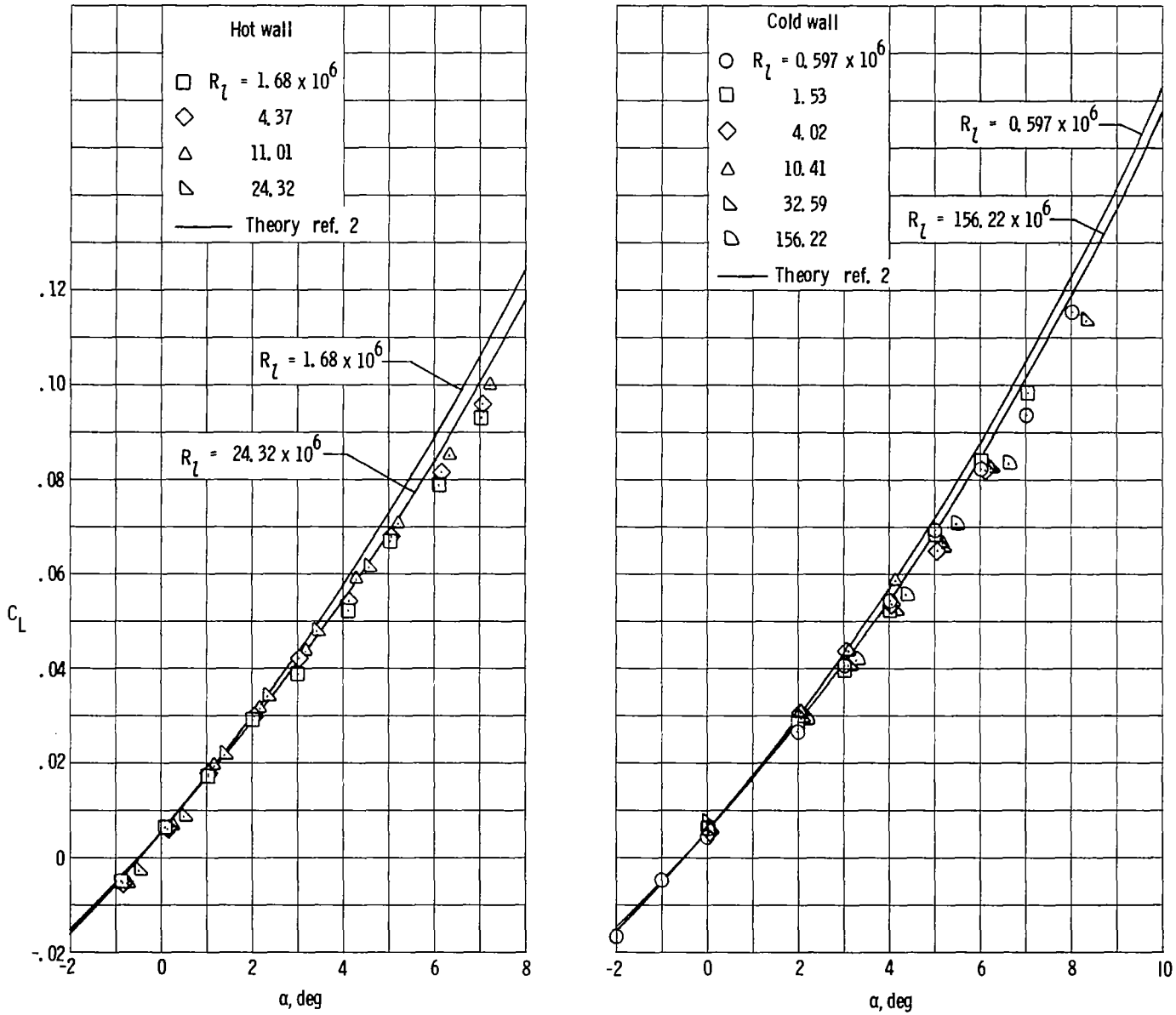

(c) Lift.

Figure 4.- Continued.

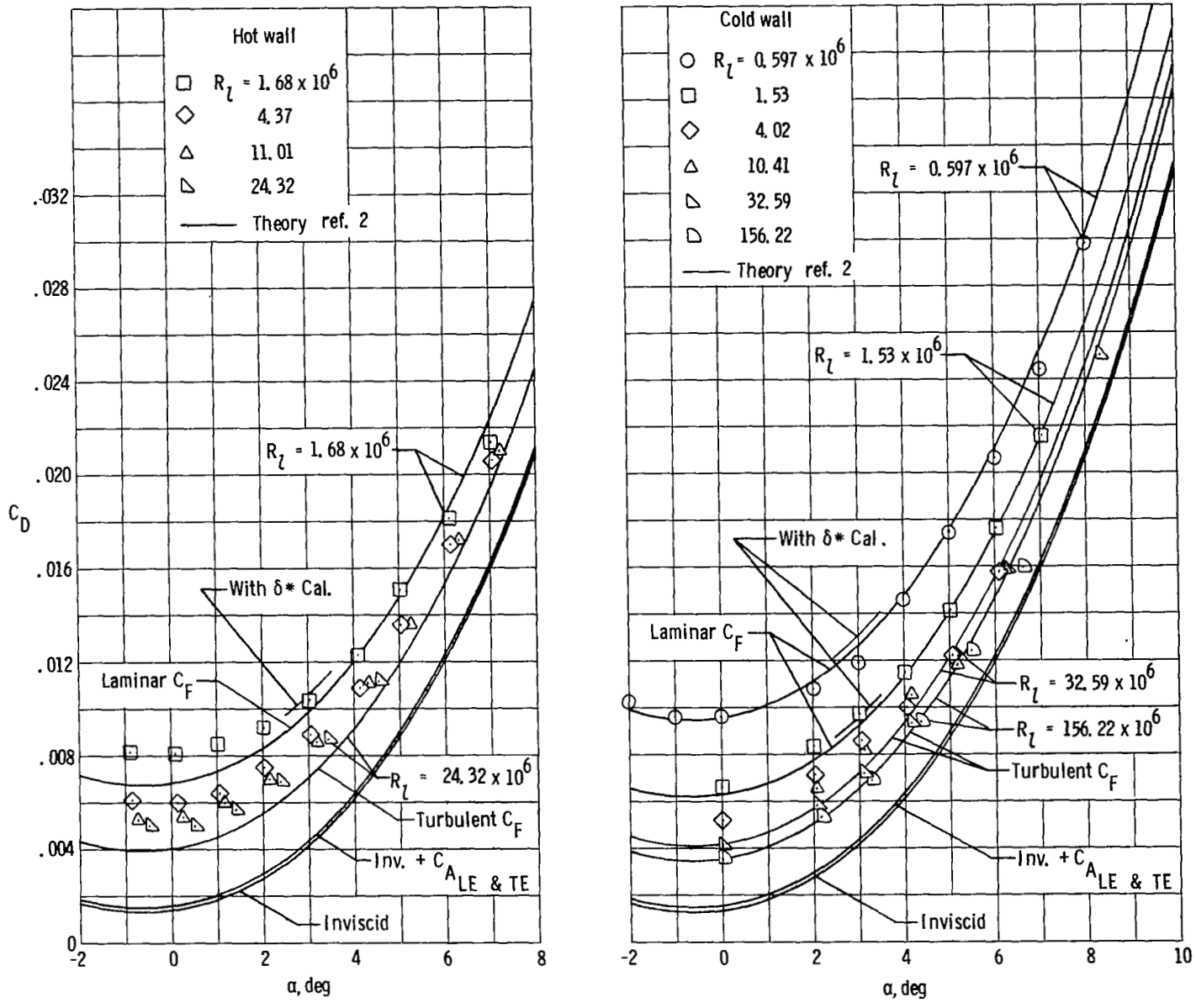

(d) Drag.

Figure 4.- Continued.

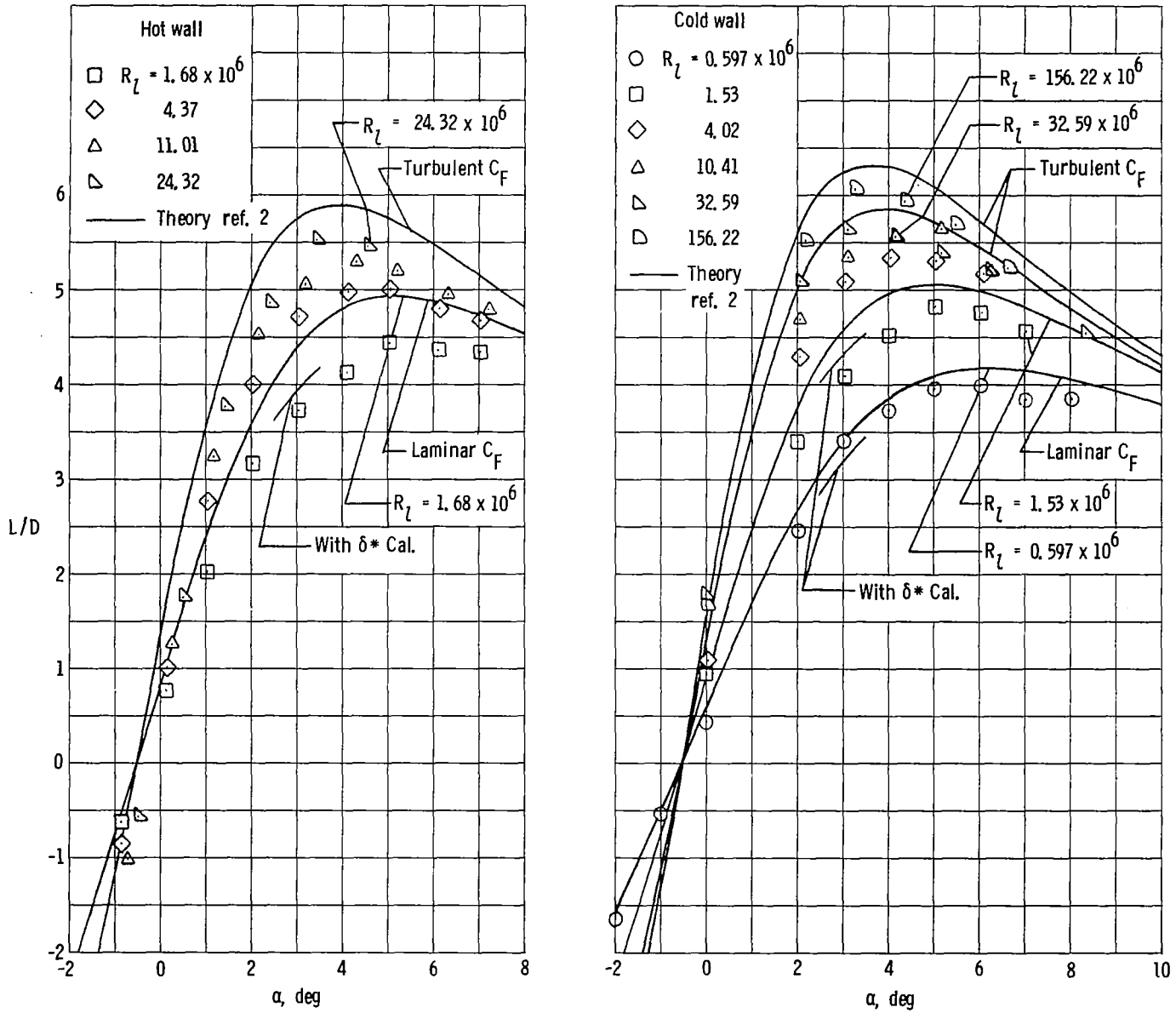

(e) Lift-drag ratio.

Figure 4.- Continued.

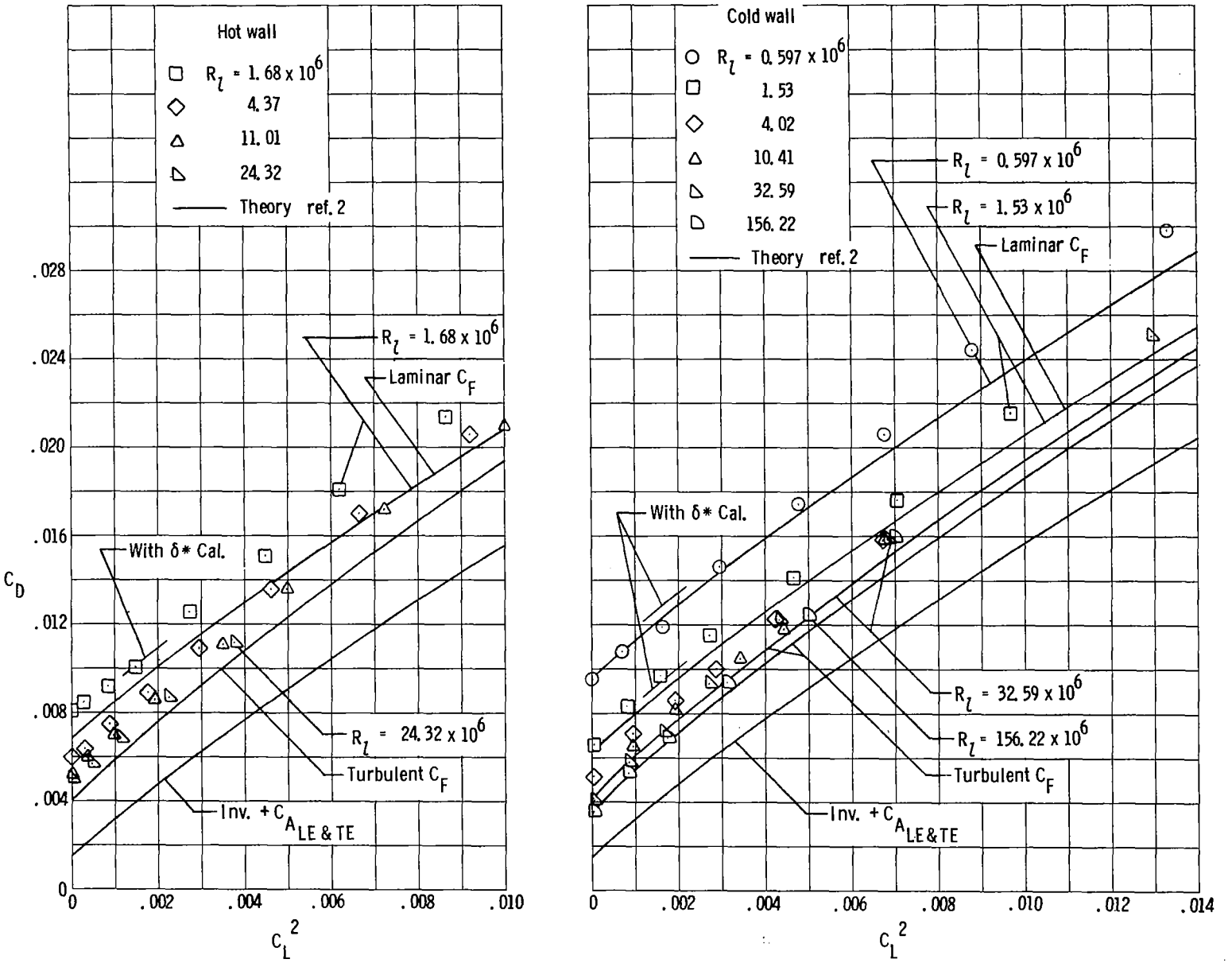

(f) Drag due to lift.

Figure 4.- Continued.

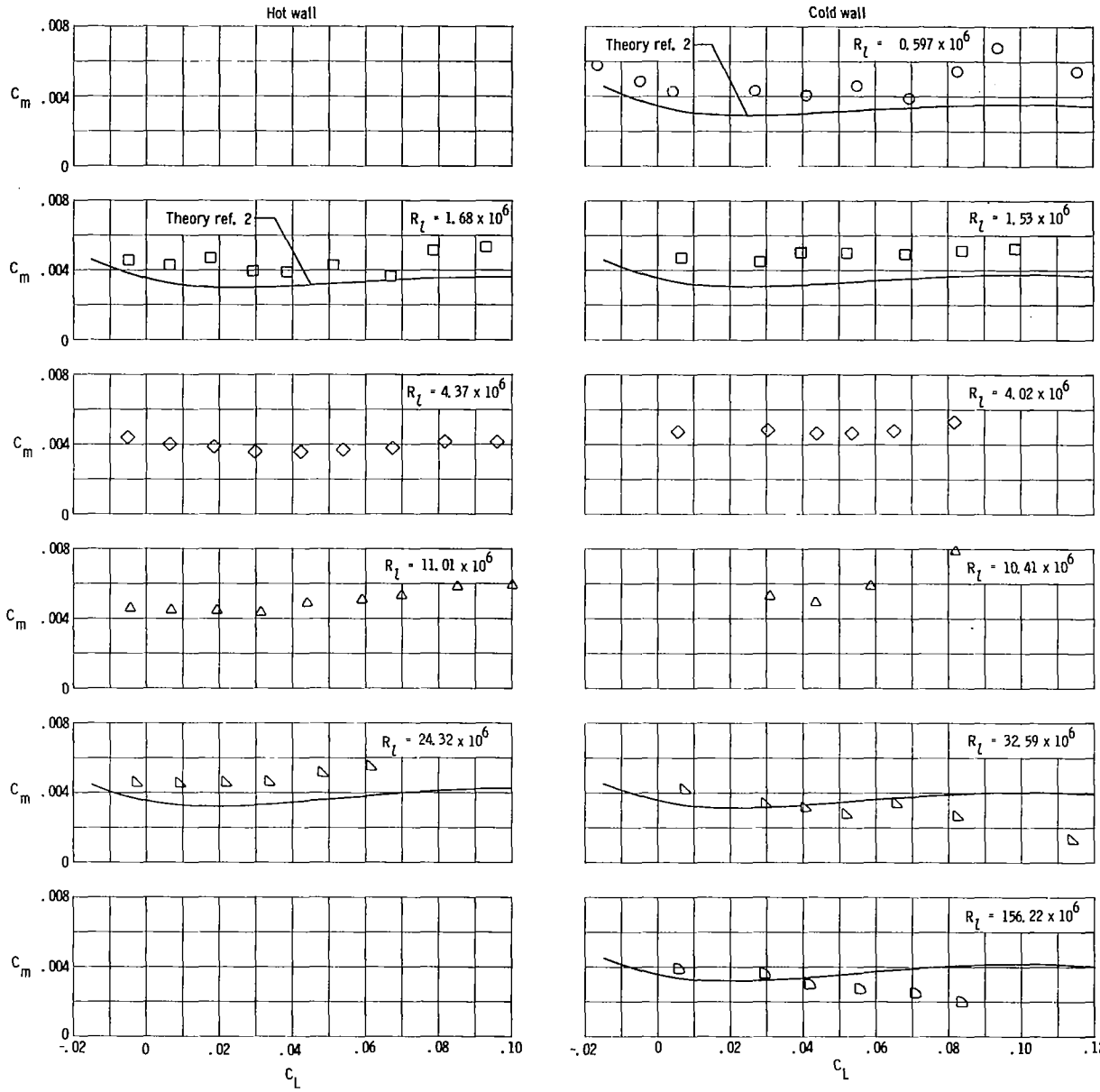

(g) Longitudinal stability.

Figure 4.- Concluded.

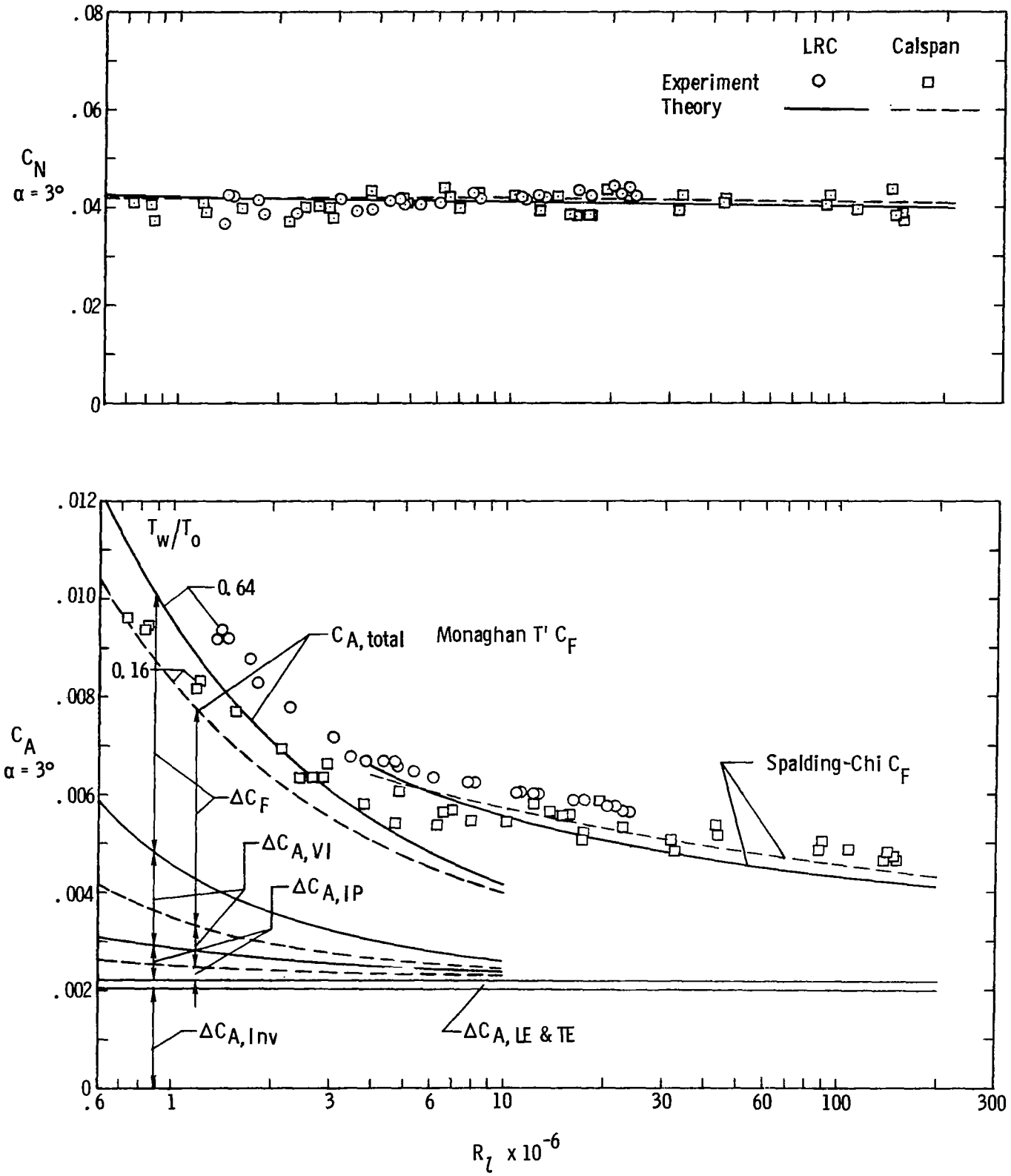

Figure 5.- Comparison of experimental normal- and axial-force coefficients with calculations from the GHABAP on the fuselage-wing configuration. $\alpha = 3°$; $M_\infty \approx 8$.

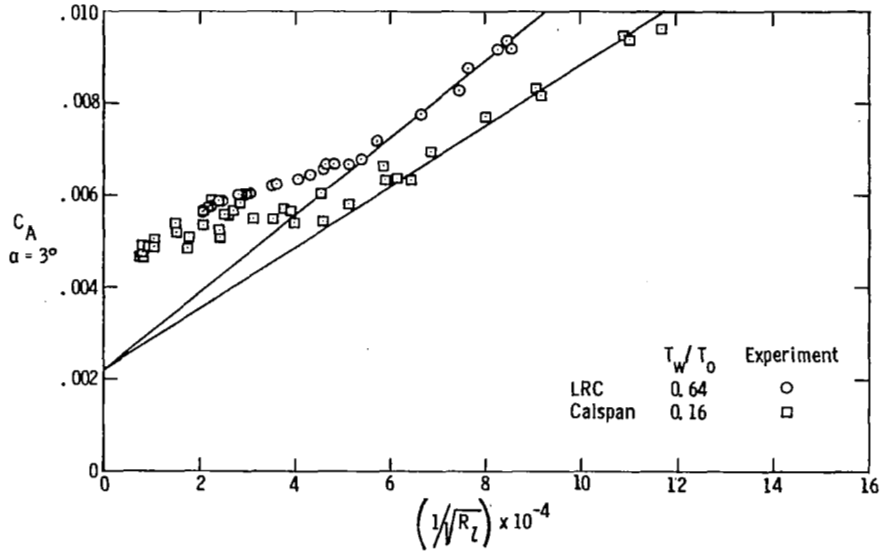

(a) Extrapolation of laminar data.

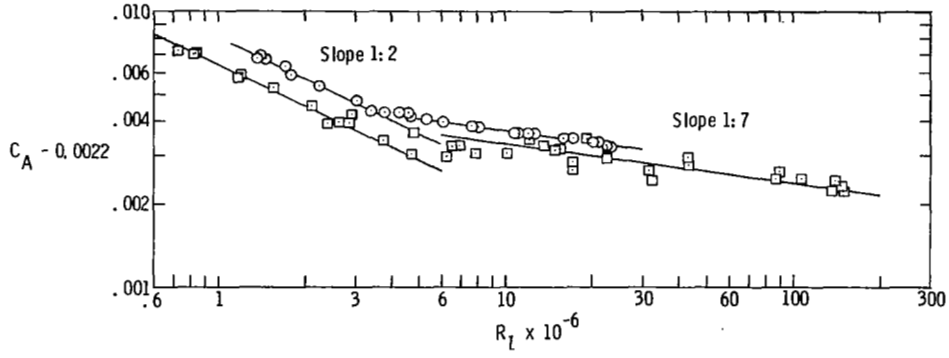

(b) Reynolds number root determination.

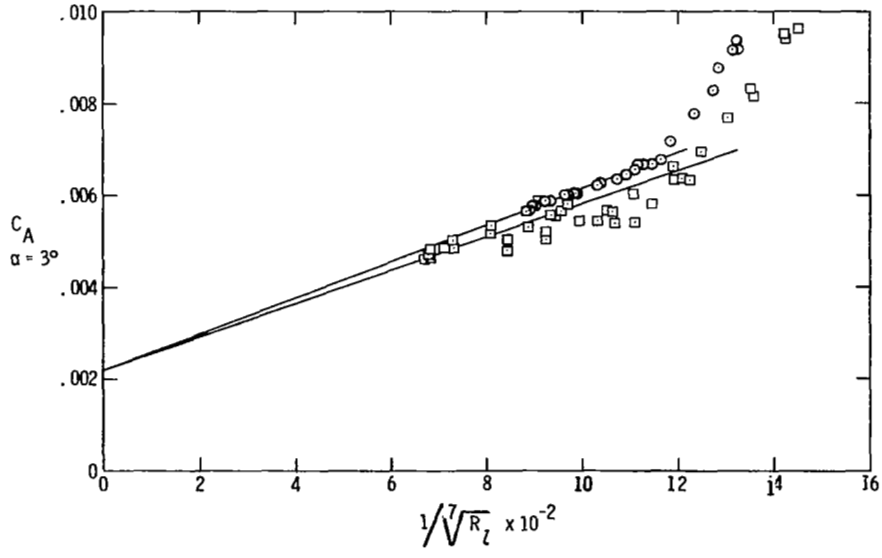

(c) Extrapolation of turbulent data.

Figure 6.- Extrapolation of data to very high Reynolds numbers. $\alpha = 3°$; $M_\infty \approx 8$.

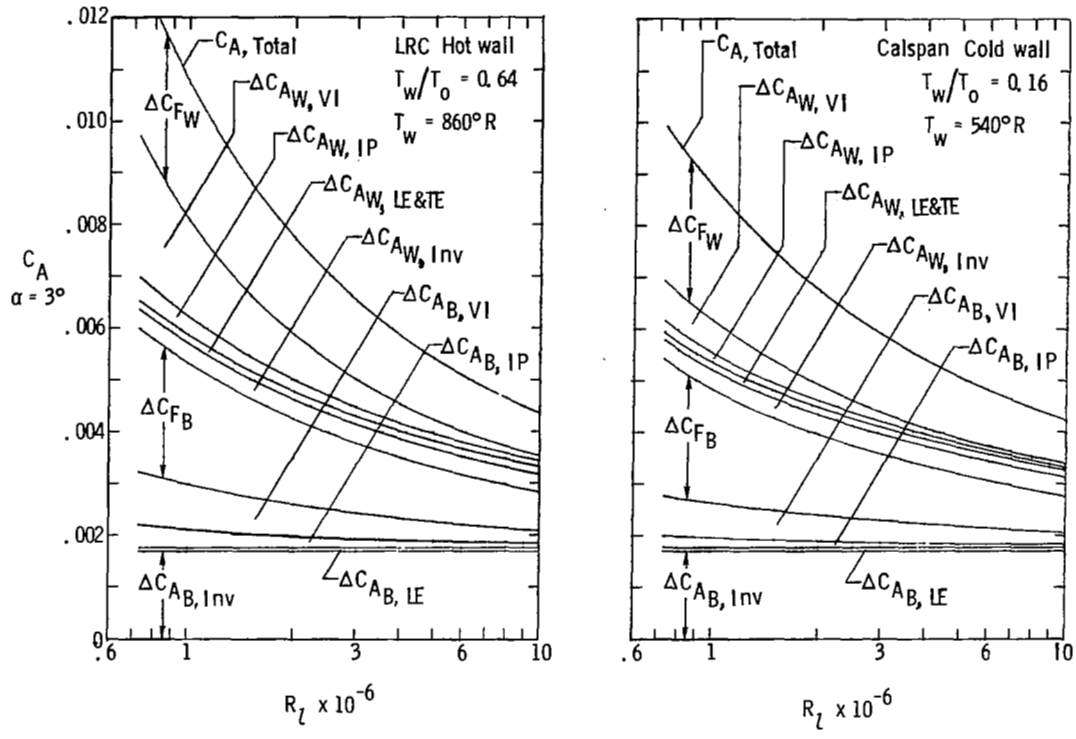

(a) Buildup of laminar theory.

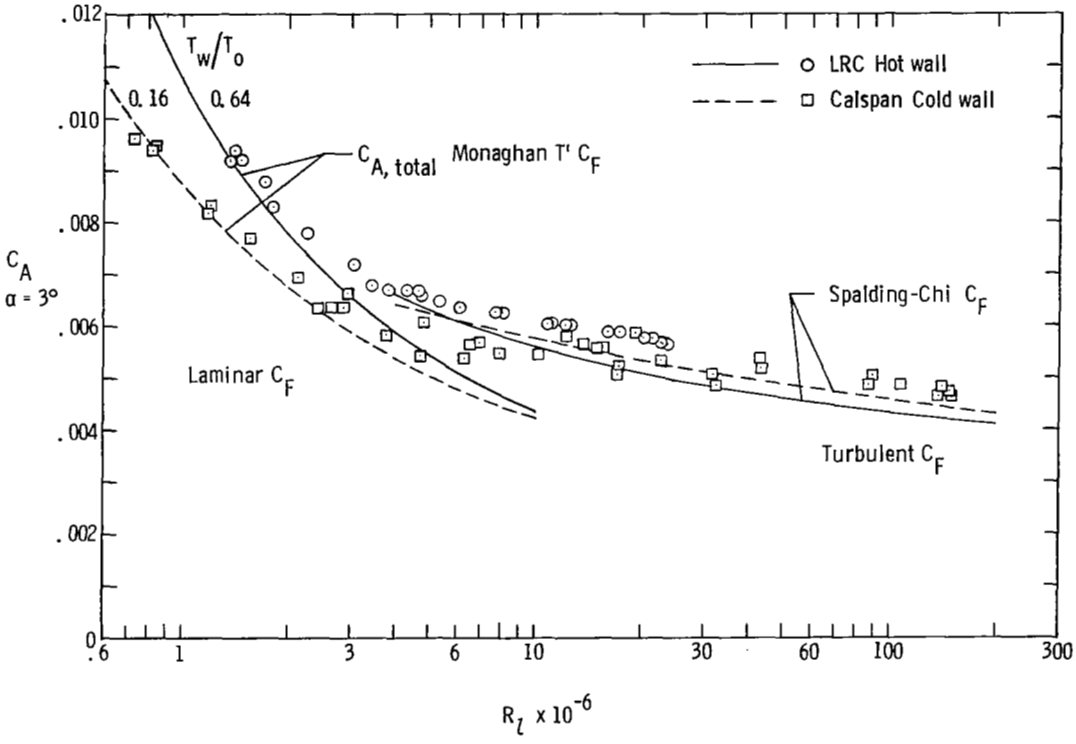

(b) Comparison of experiment and theory.

Figure 7.- Buildup of present laminar predictions of axial-force coefficient at two wall temperature ratios and comparison with experimental data. $\alpha = 3°$; $M_\infty \approx 8$.

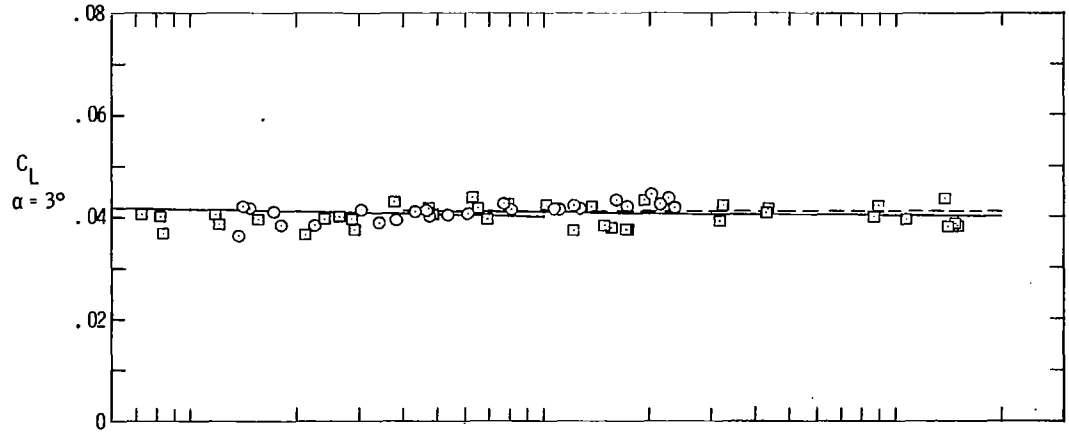

(a) Lift coefficient.

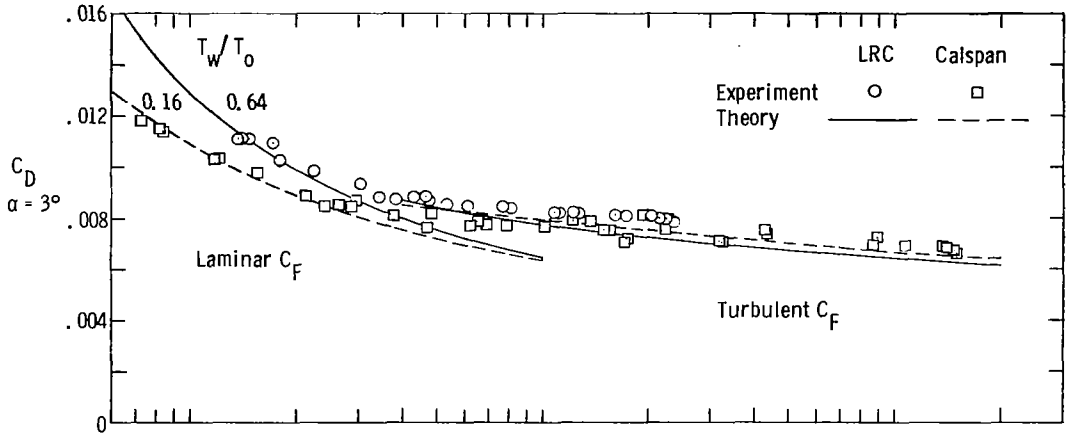

(b) Drag coefficient.

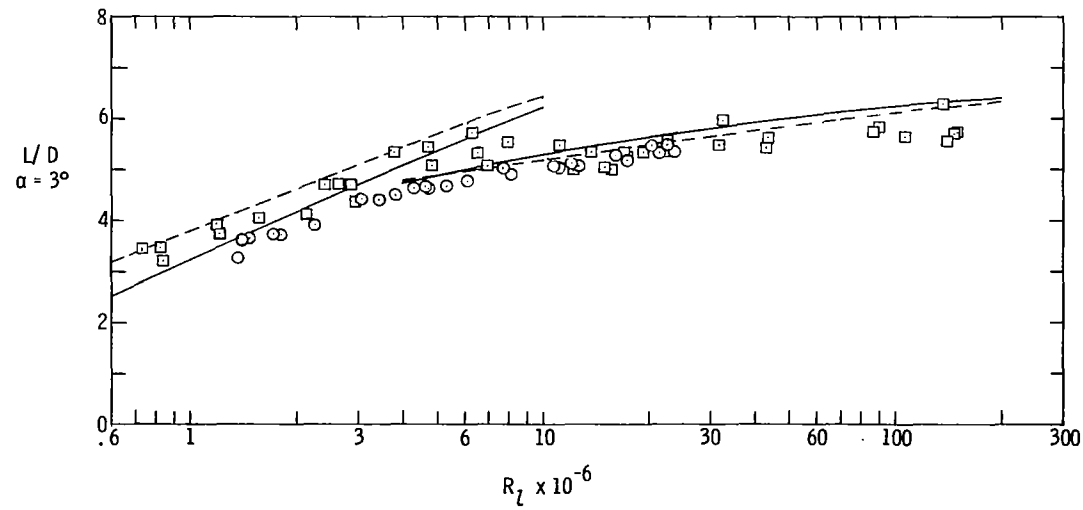

(c) Lift-drag ratio.

Figure 8.- Comparison of experimental lift, drag, and lift-drag ratio at two wall temperature ratios with improved theory. $\alpha = 3°$; $M_\infty \approx 8$.

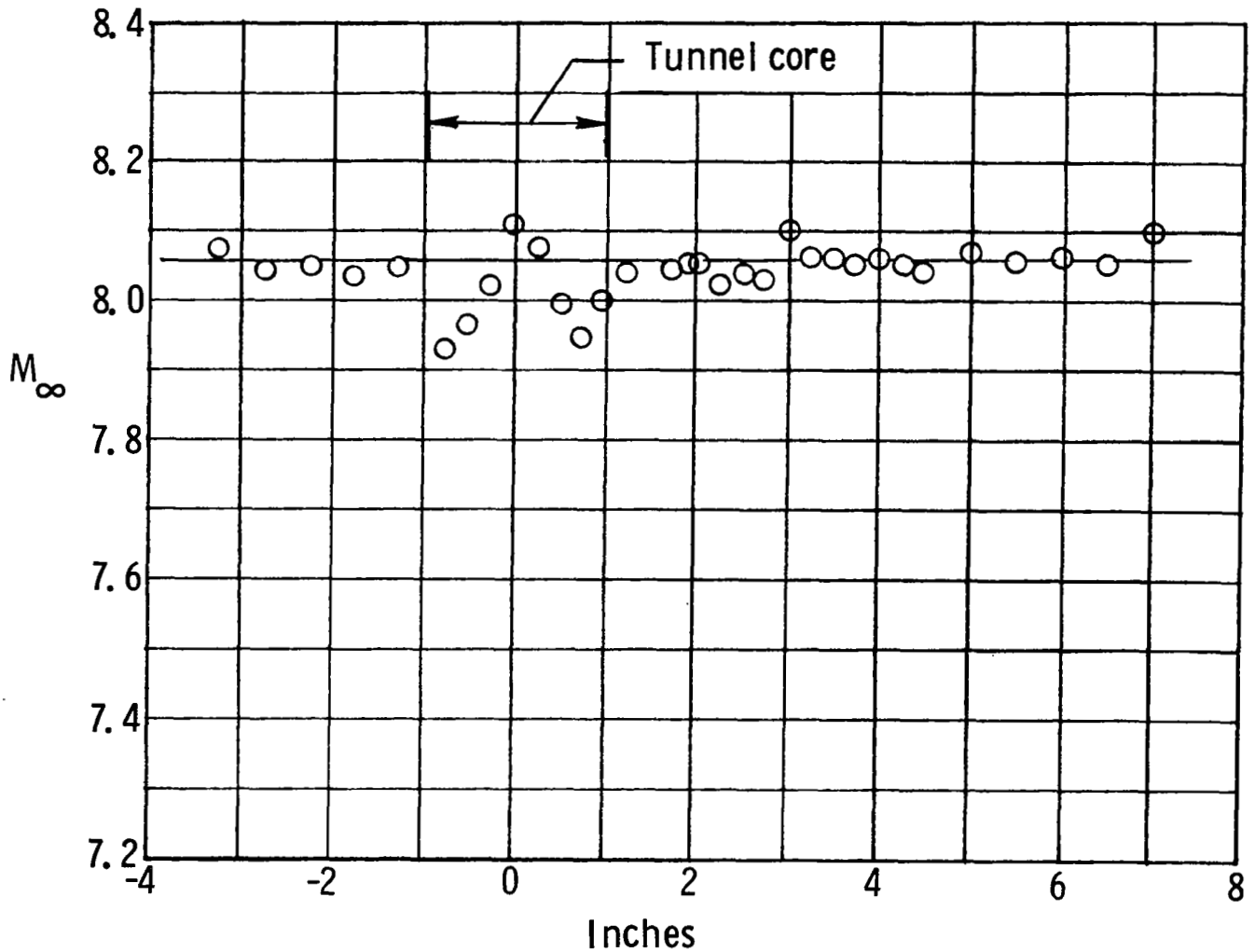

Figure 9.- Vertical Mach number distribution (taken from ref. 19) through test-section centerline of the Langley Mach 8 Variable-Density Tunnel. P_o = 2515 psia; T_o = 1460°R.

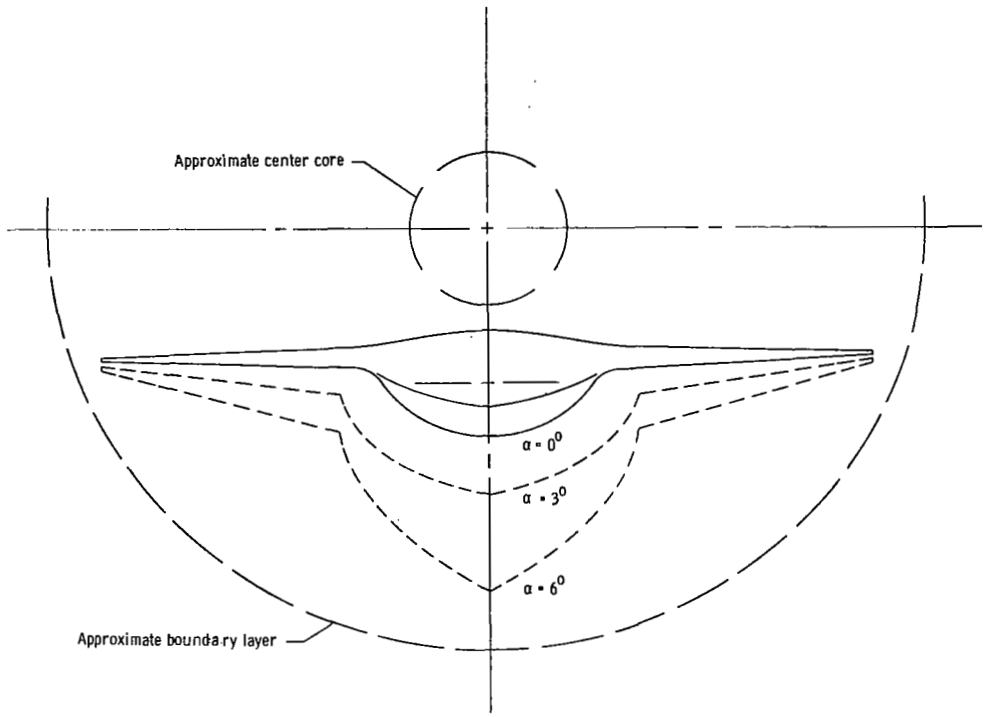

(a) Schematic downstream view of test-section area utilized for present tests.

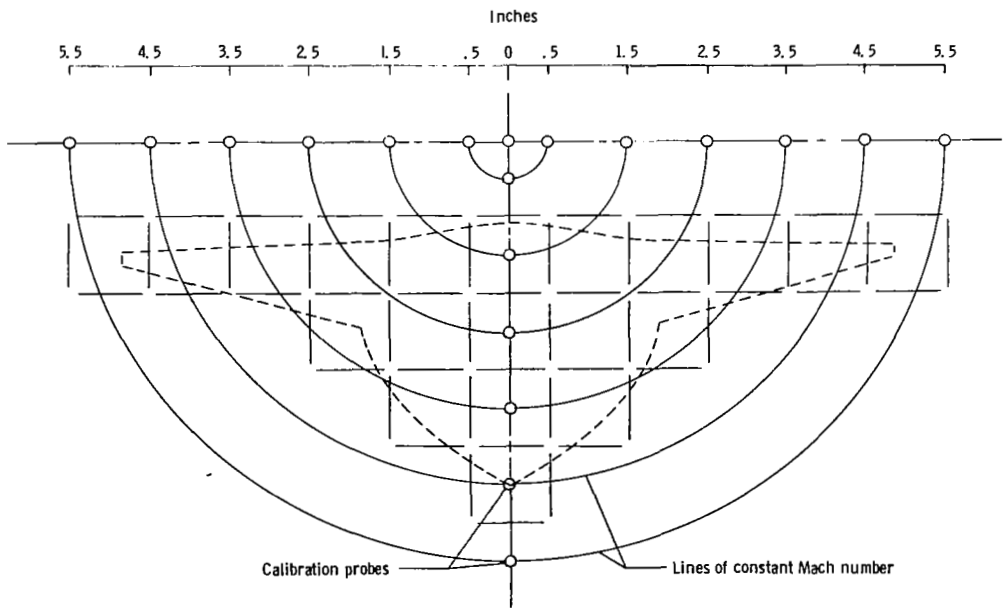

(b) Radial lines of constant calibrated Mach number superimposed on frontal view of model.

Figure 10.- Test region and calibration scheme in the Langley Mach 8 Variable-Density Tunnel.

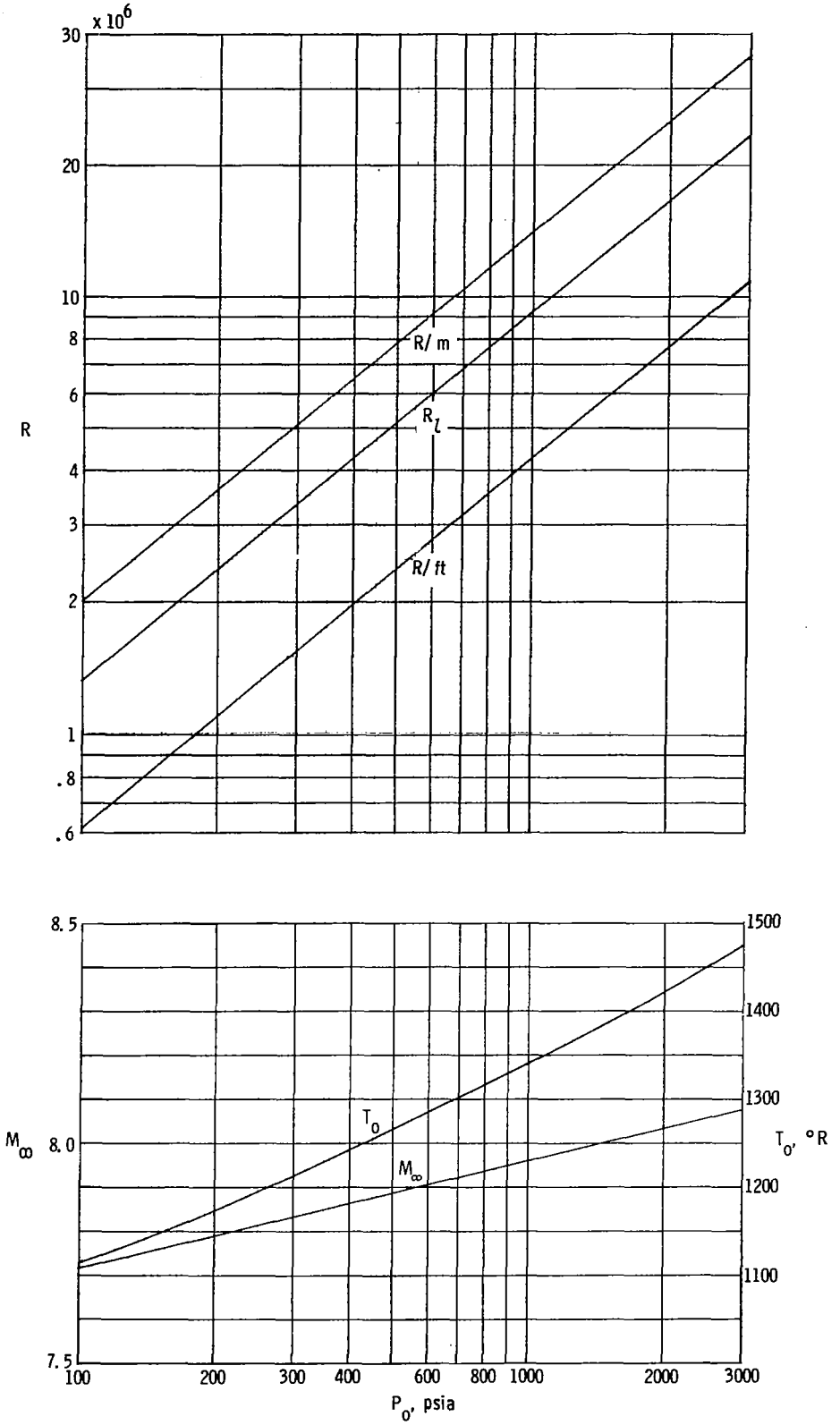

Figure 11.- Calibration Reynolds number and Mach number for stagnation pressure range in the Langley Mach 8 Variable-Density Tunnel.

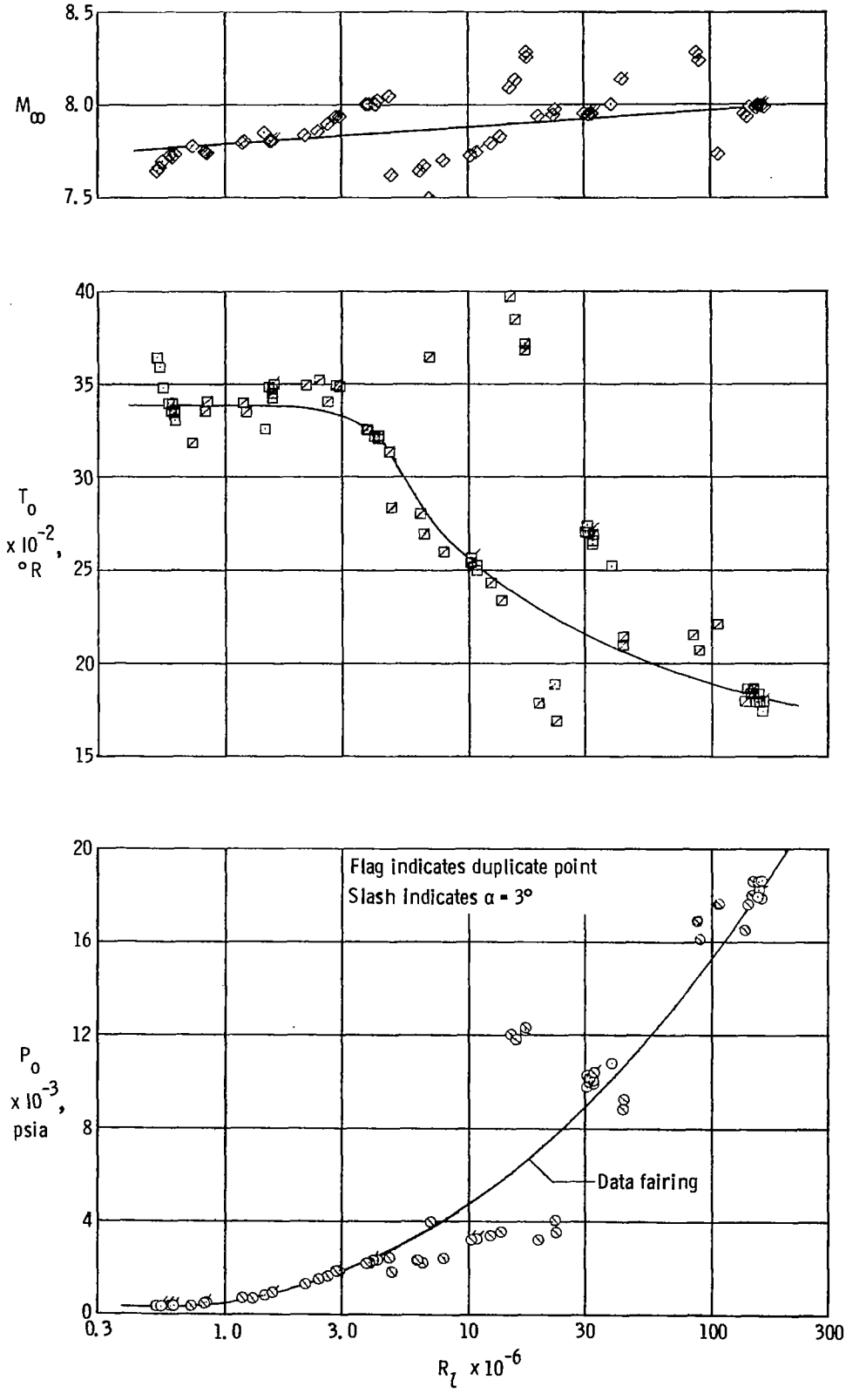

Figure 12.- Test conditions for present study in the Calspan 96-Inch Shock Tunnel.

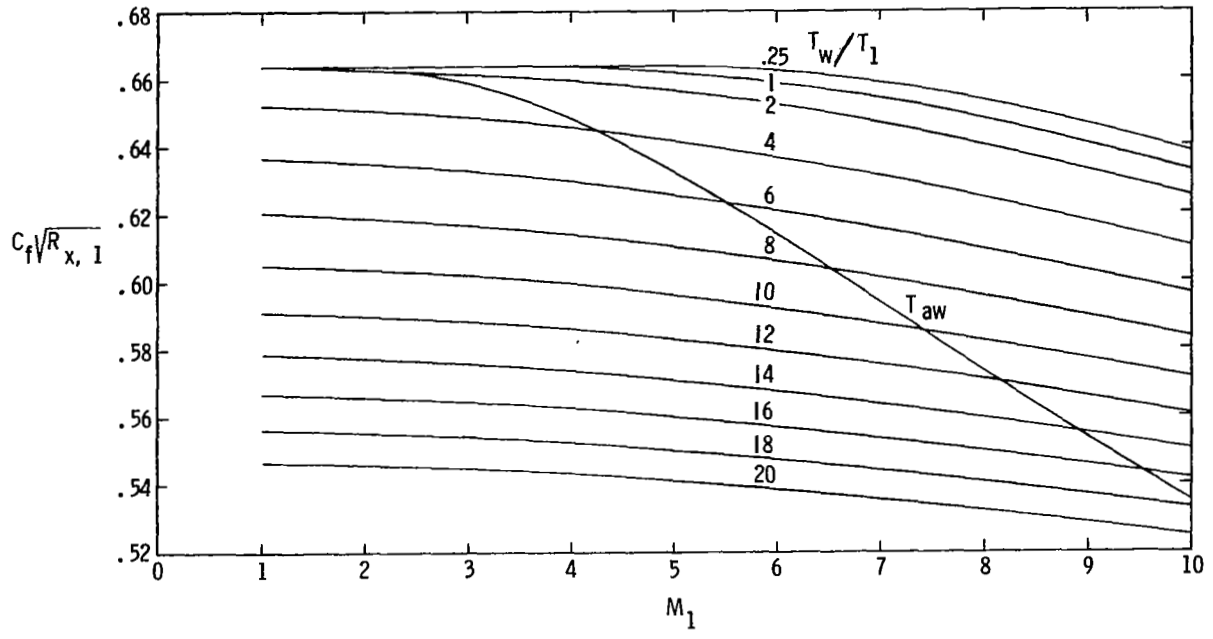

(a) Variation with local Mach number. T_1 = 100°R.

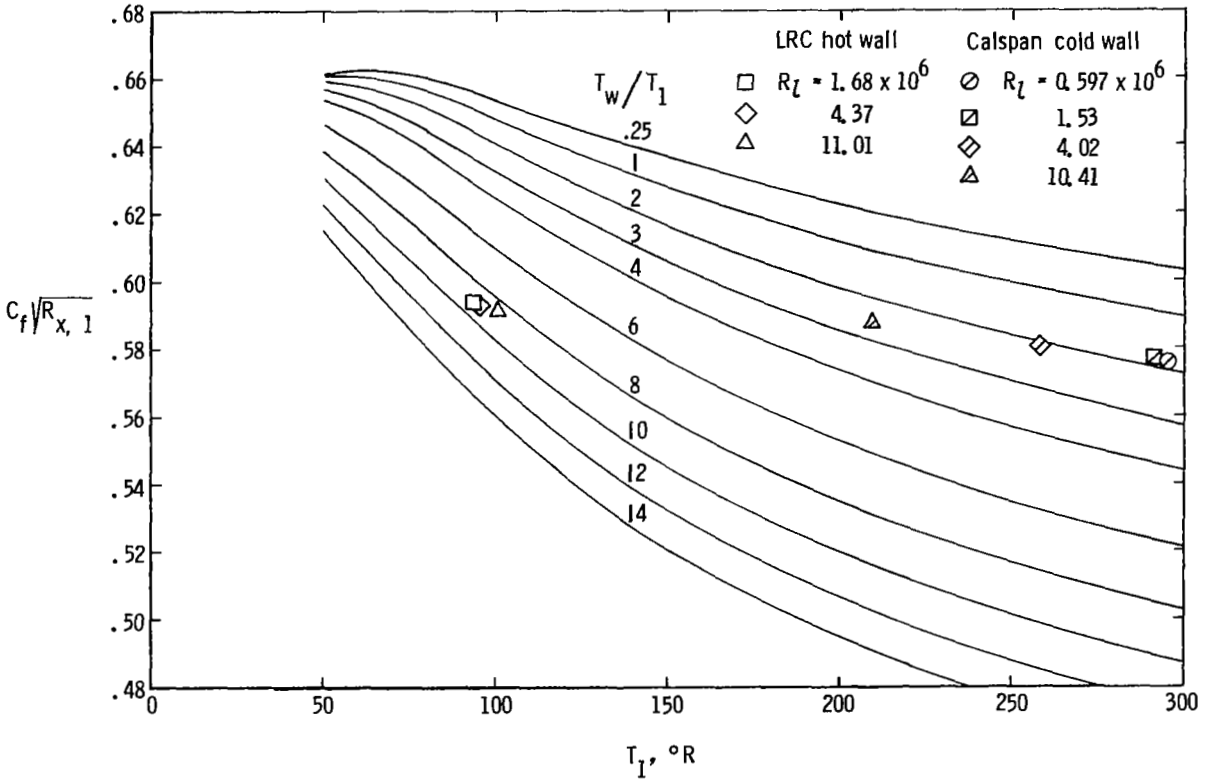

(b) Variation with local temperature. M_1 = 8.

Figure 13.- Variation of local flat-plate laminar skin friction with local Mach number and local temperature.

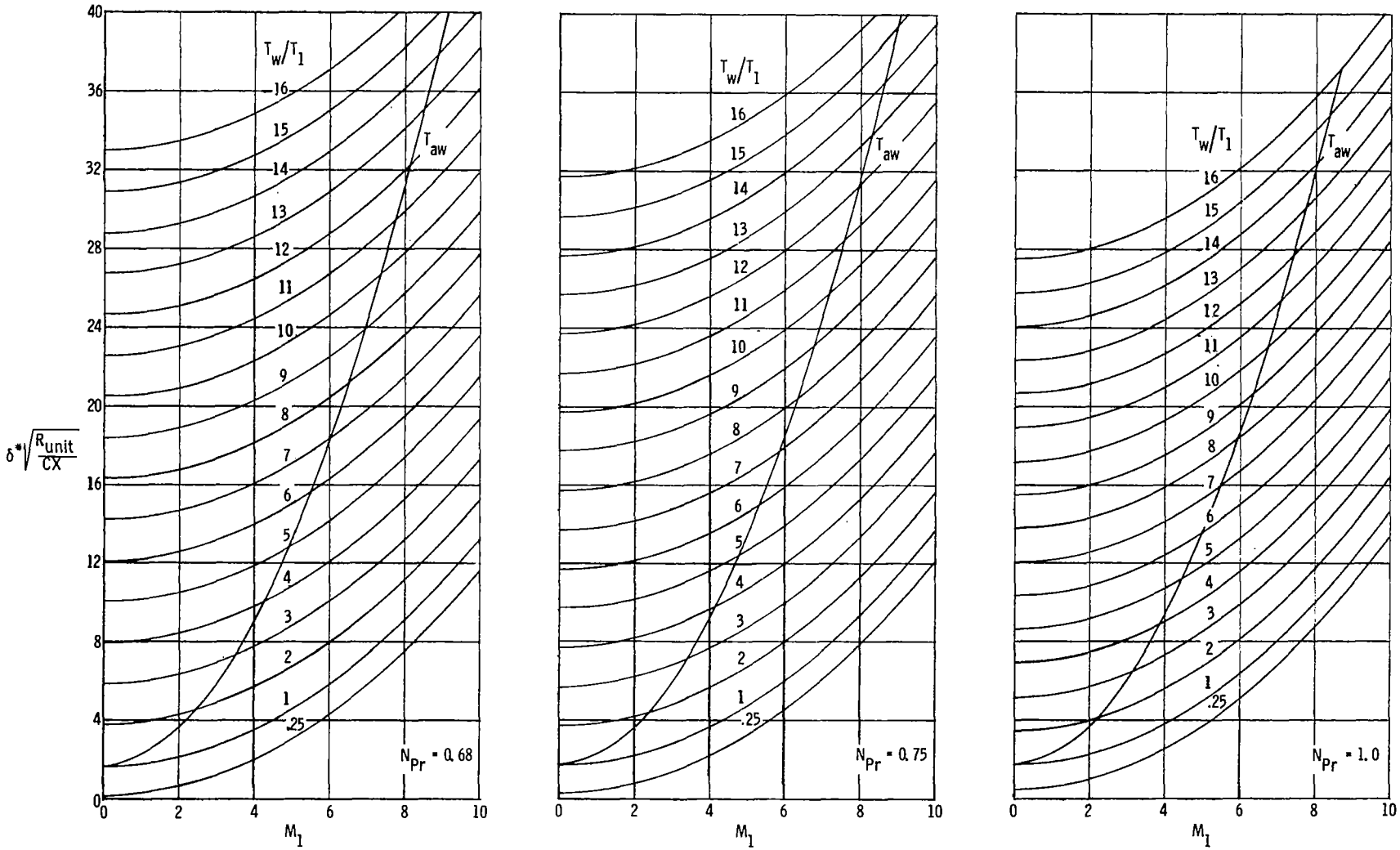

Figure 14.- Variation of laminar-boundary-layer displacement thickness (ref. 8).

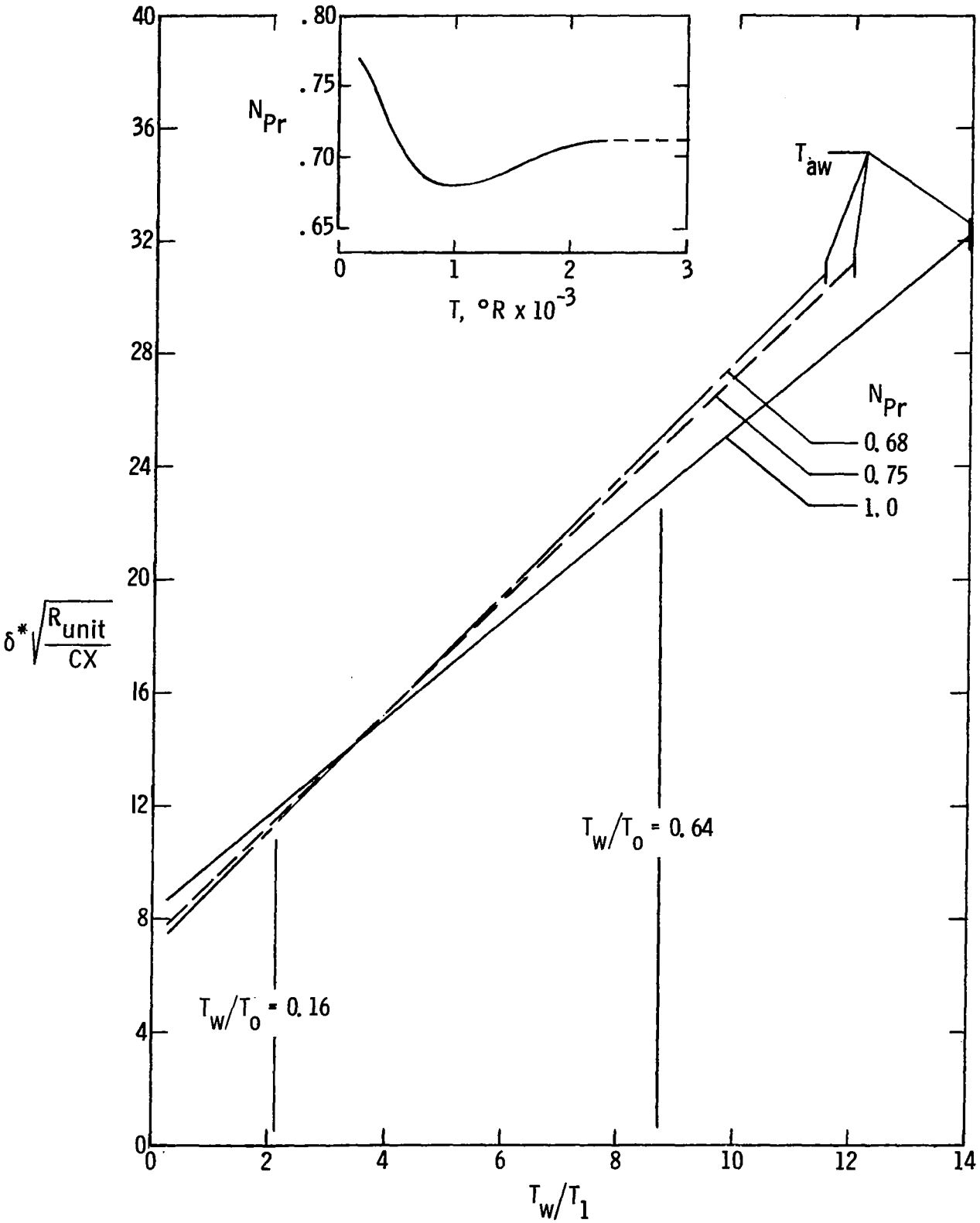

Figure 15.- Variation of boundary-layer displacement thickness (ref. 8) on a flat plate with temperature ratio for various Prandtl numbers and $M_1 = 8$.

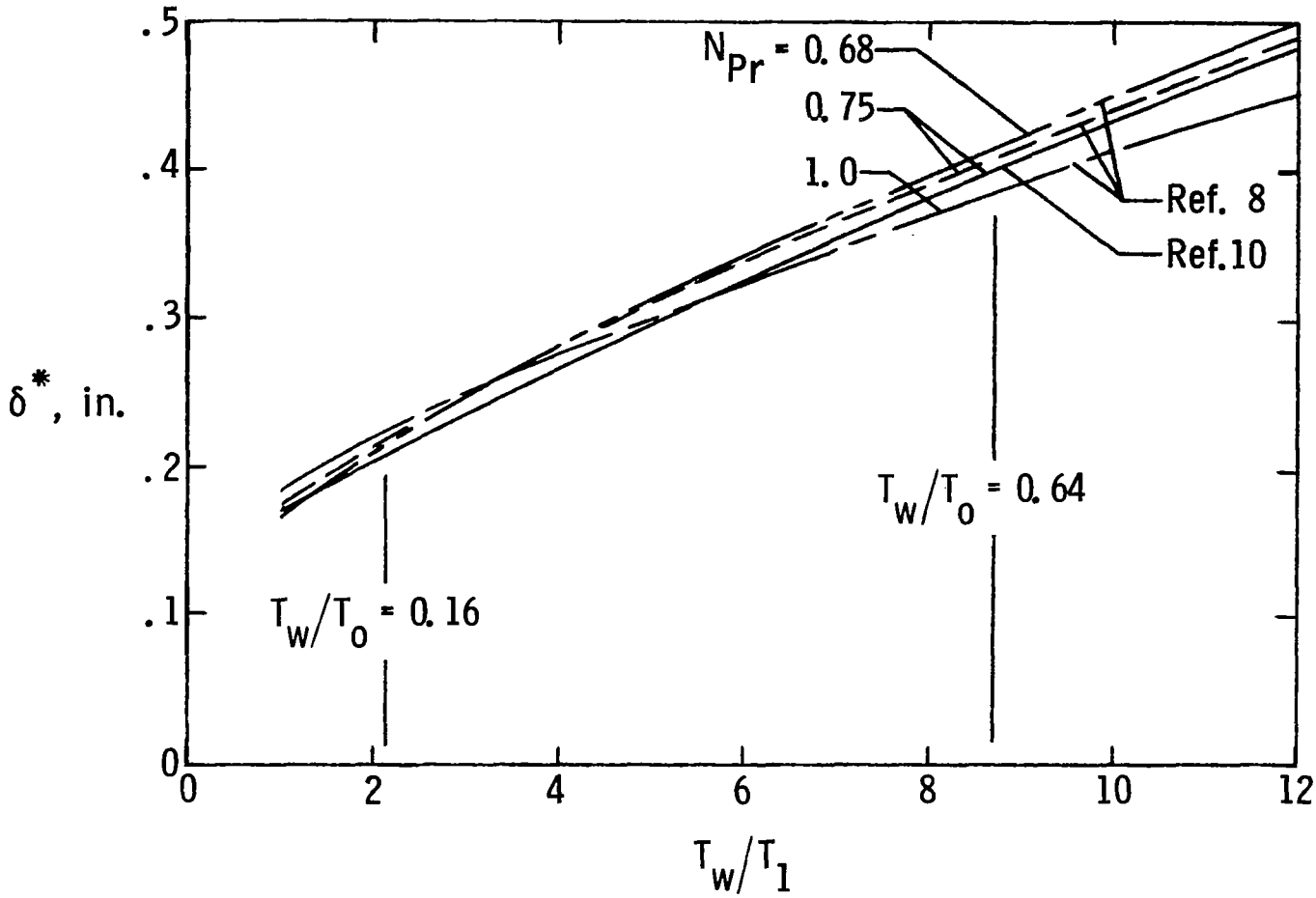

Figure 16.- Variation of calculated boundary-layer displacement thickness on a flat plate by two theoretical methods at $M_1 = 8$ and $R_{x,1} = 0.384 \times 10^6$.

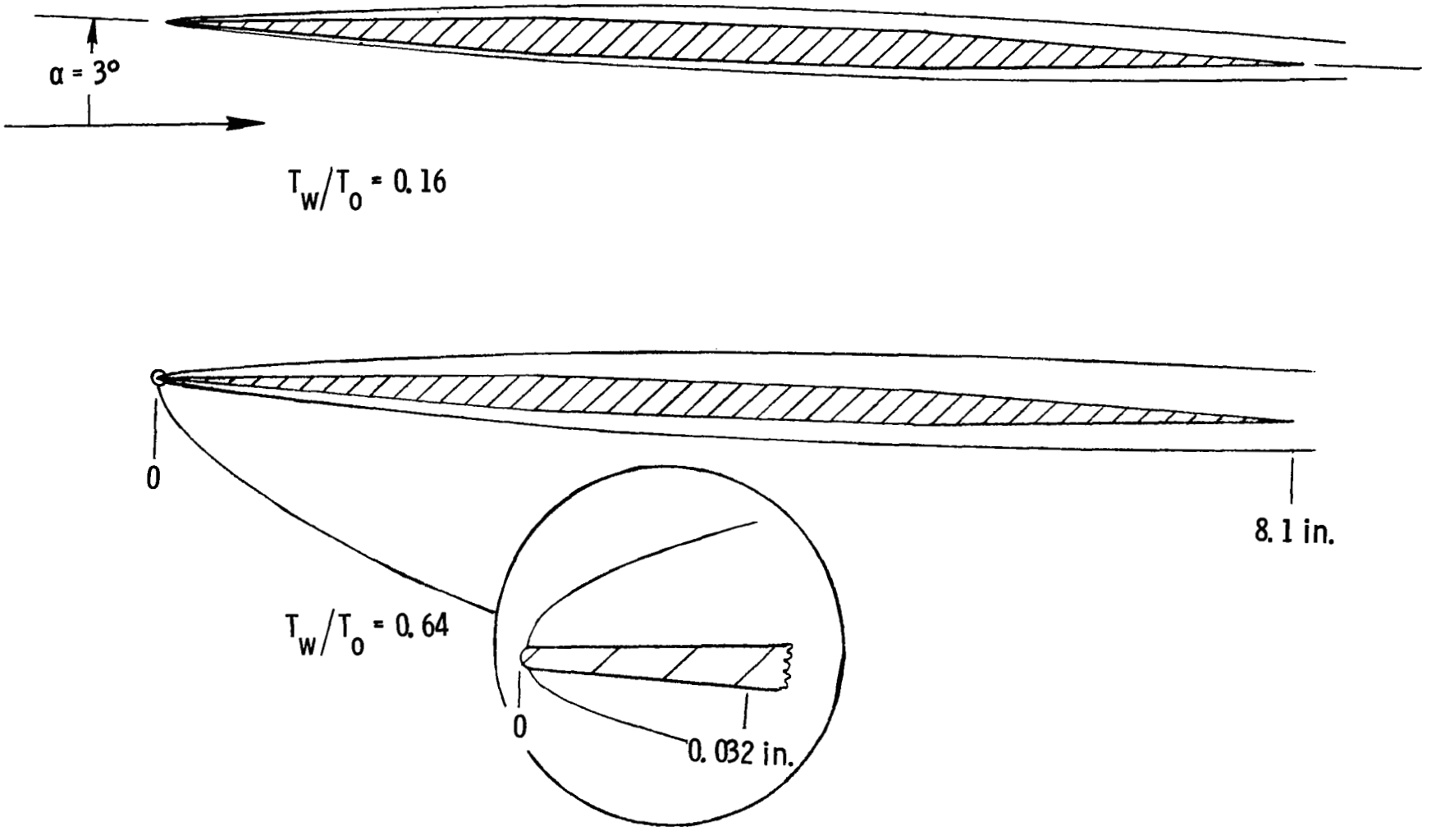

Figure 17.- Variation of calculated laminar-boundary-layer displacement thickness with wall temperature on exposed wing root chord. $M_\infty = 7.74$; $R_l = 1.4 \times 10^6$.

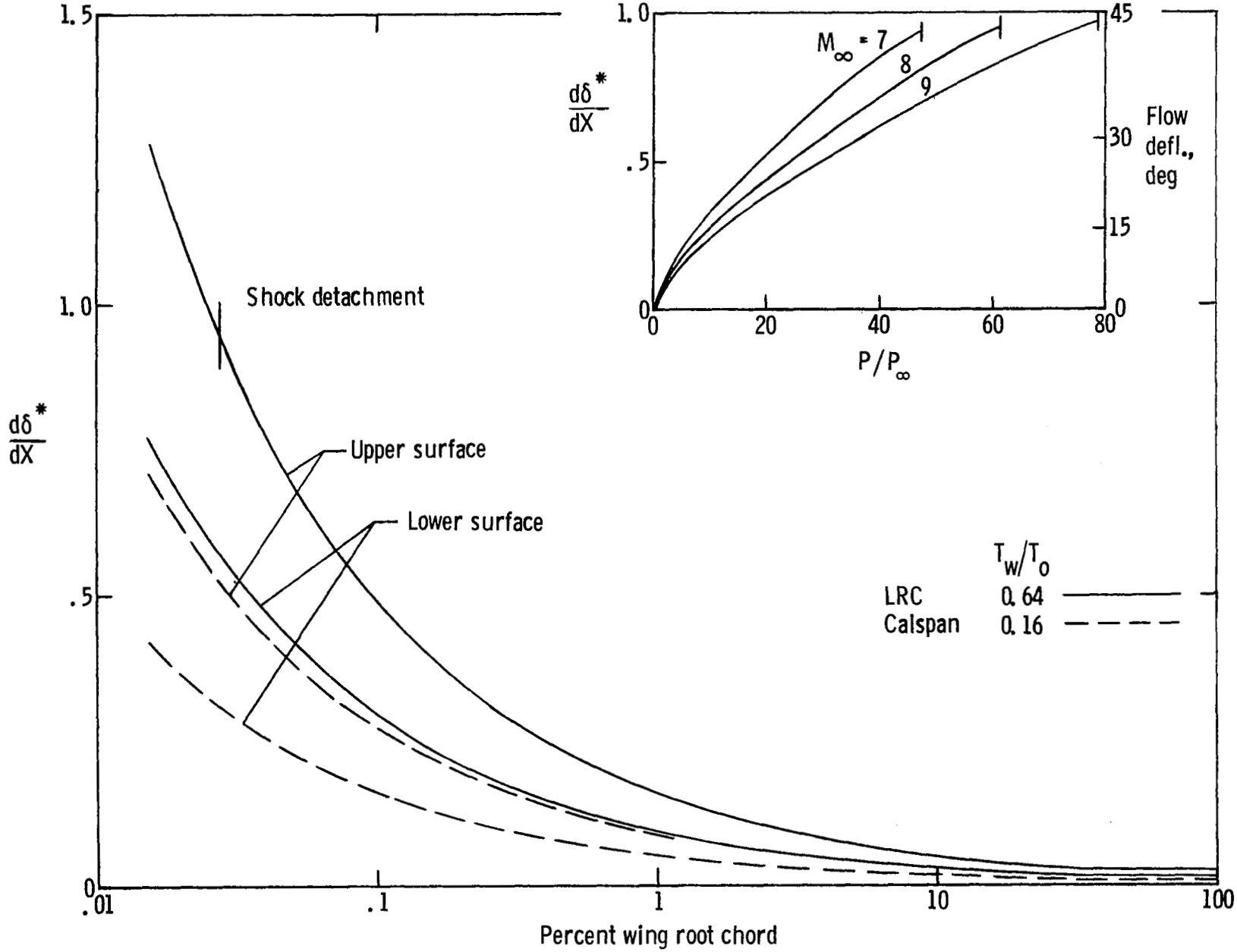

Figure 18.- Variation of the slope of boundary-layer displacement thickness with exposed wing root chord and resulting tangent-wedge pressure. $R_l = 1.4 \times 10^6$; $M_\infty = 8$.

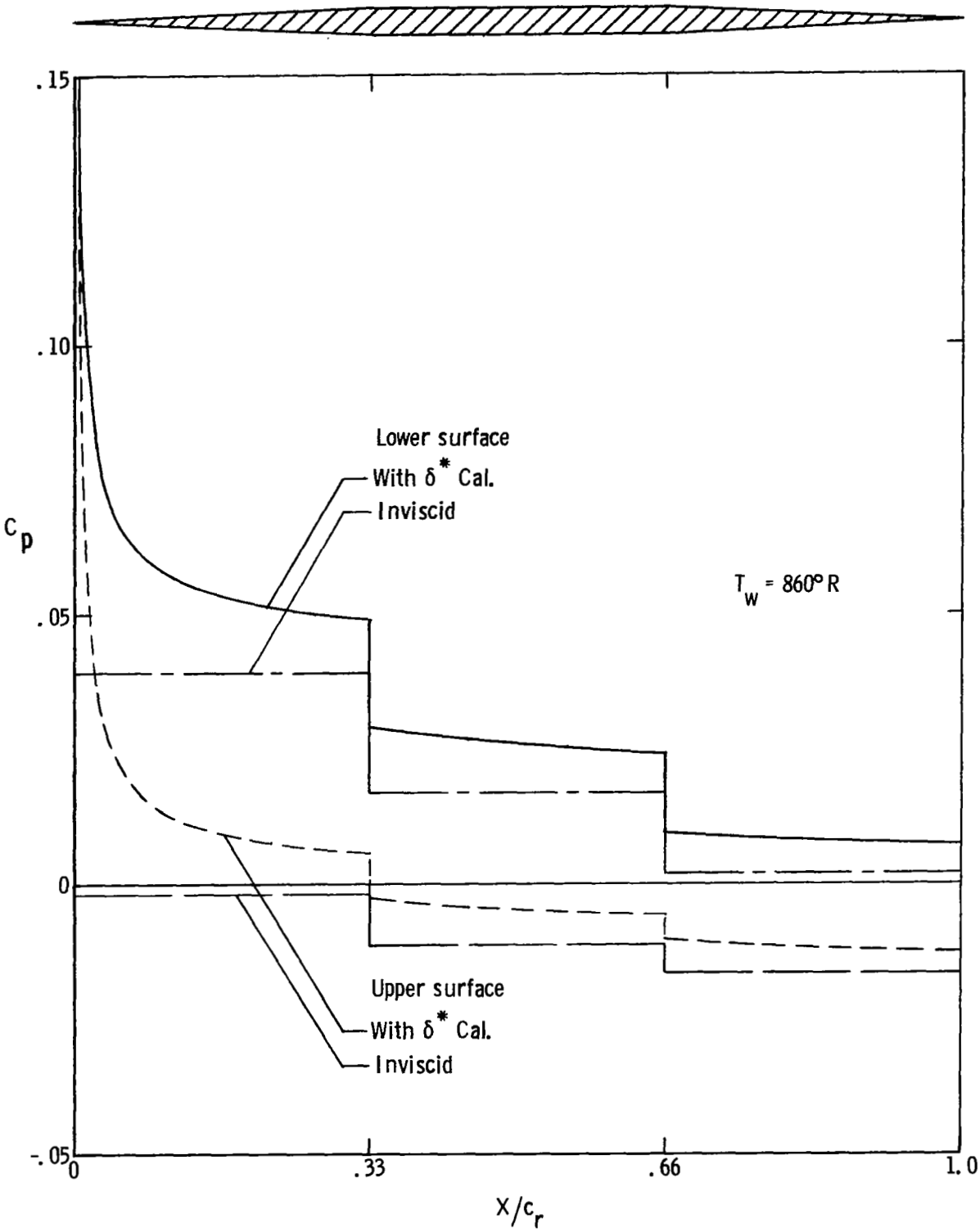

(a) Variation of pressure coefficient on the exposed wing root chord.

Figure 19.- Typical calculated wing pressure distributions. $M_\infty = 7.74$; $R_l = 1.4 \times 10^6$; $\alpha = 3°$.

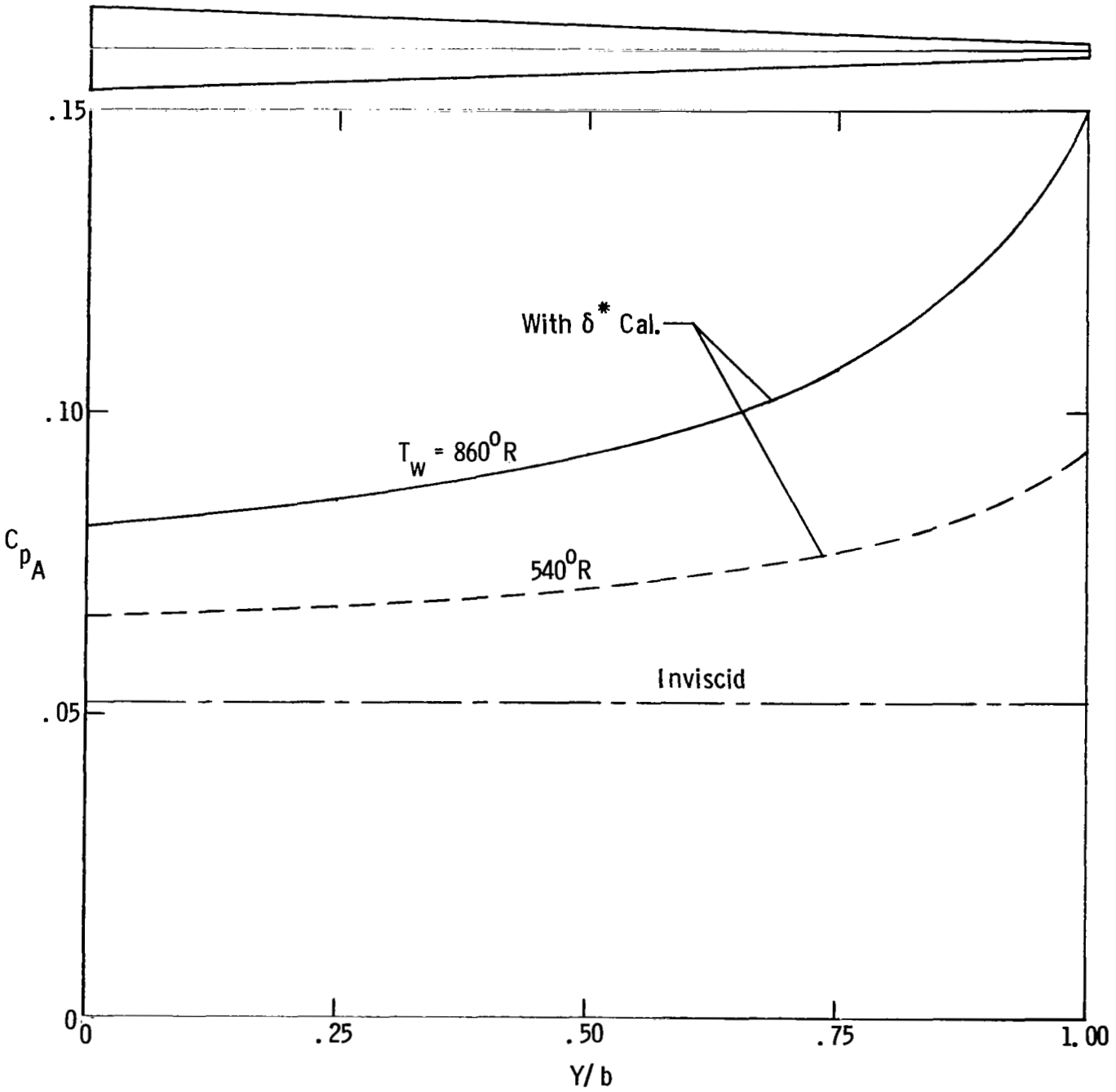

(b) Variation of axial pressure coefficient on the exposed wing semispan.

Figure 19.- Concluded.

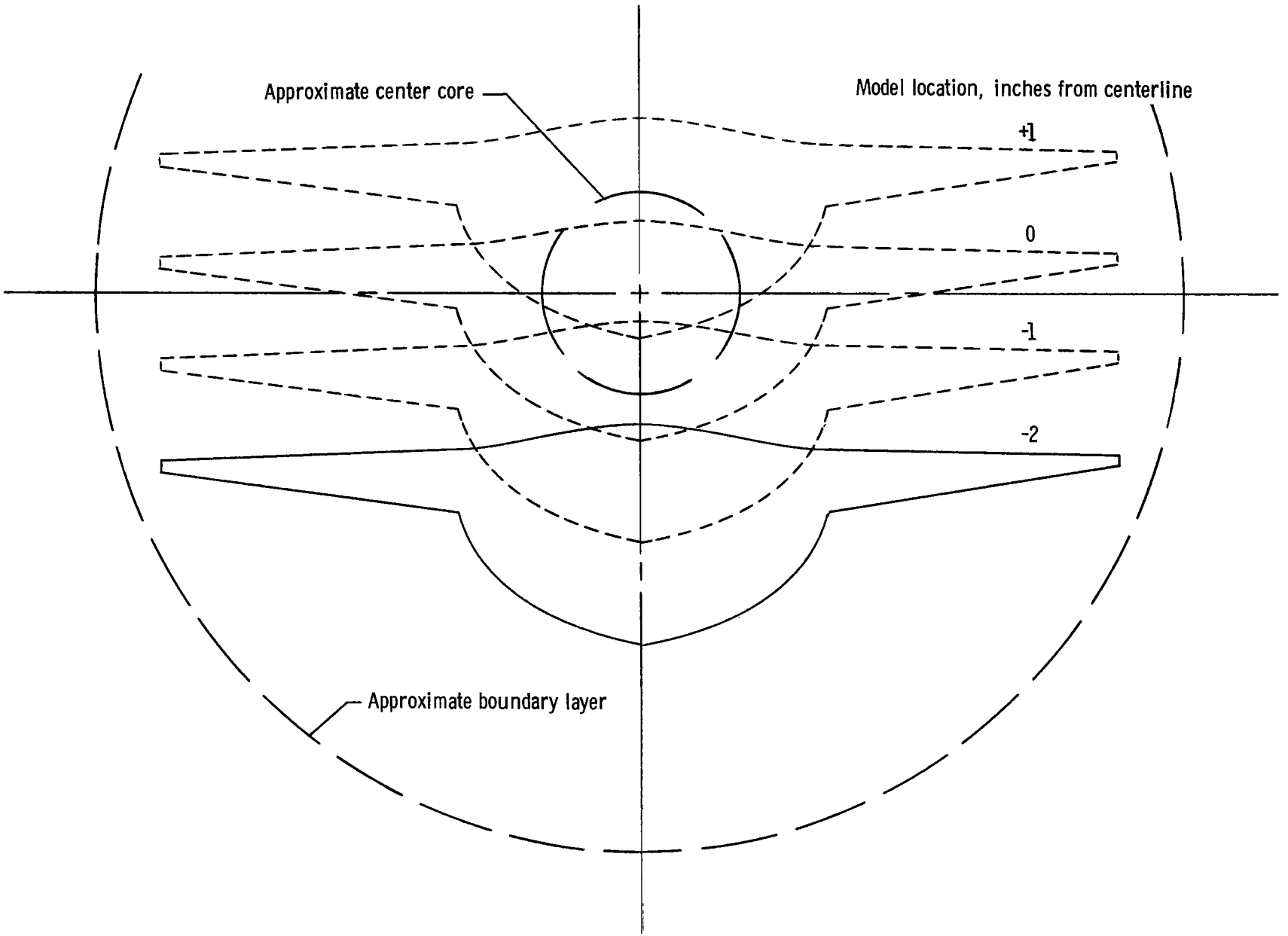

Figure 20.- Schematic downstream view of test section with model at various vertical locations in the Langley Mach 8 Variable-Density Tunnel.

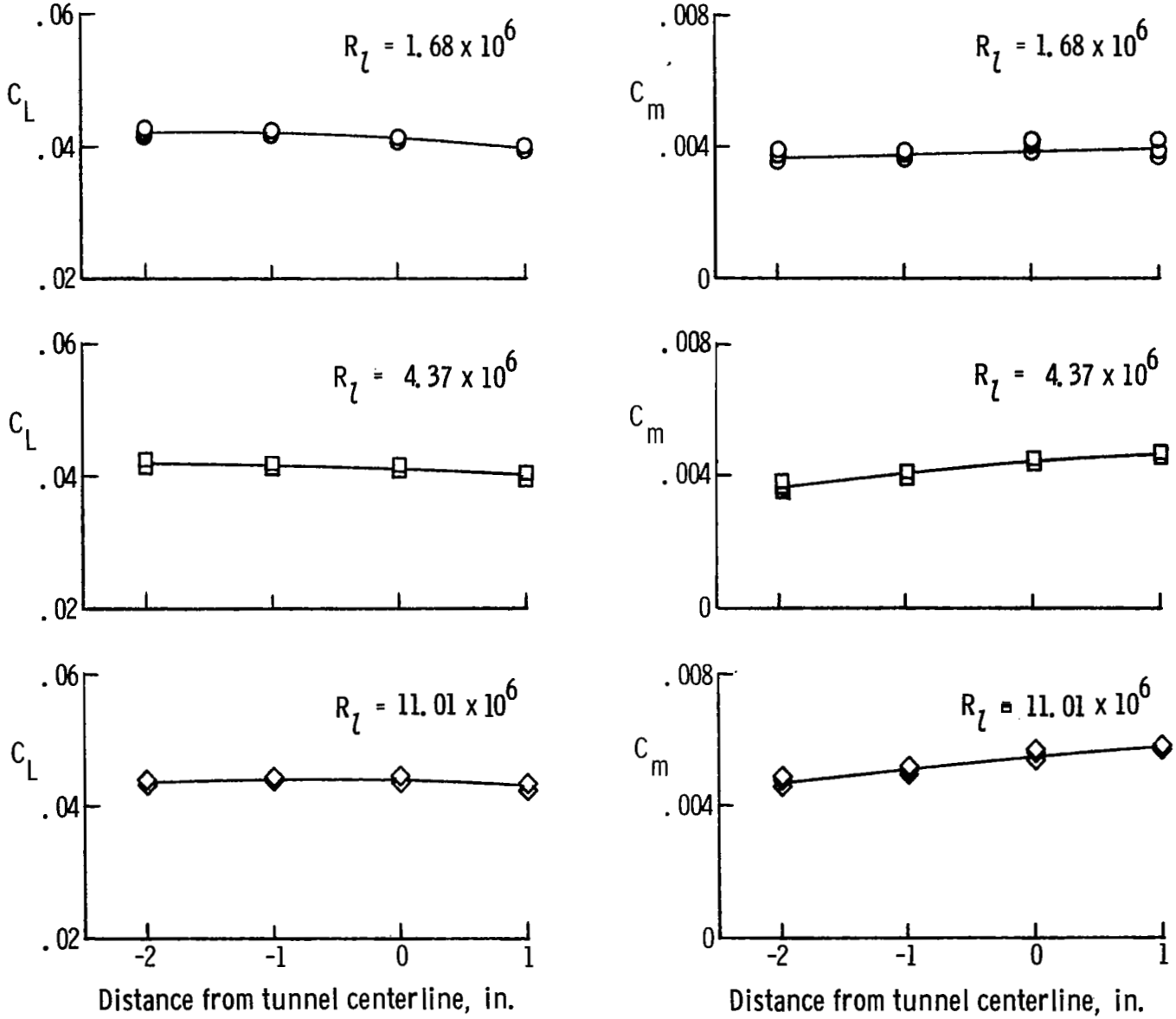

Figure 21.- Variation of lift and pitching-moment coefficients with vertical test-section location at various Reynolds numbers in the Langley Mach 8 Variable-Density Tunnel. $\alpha = 3°$.

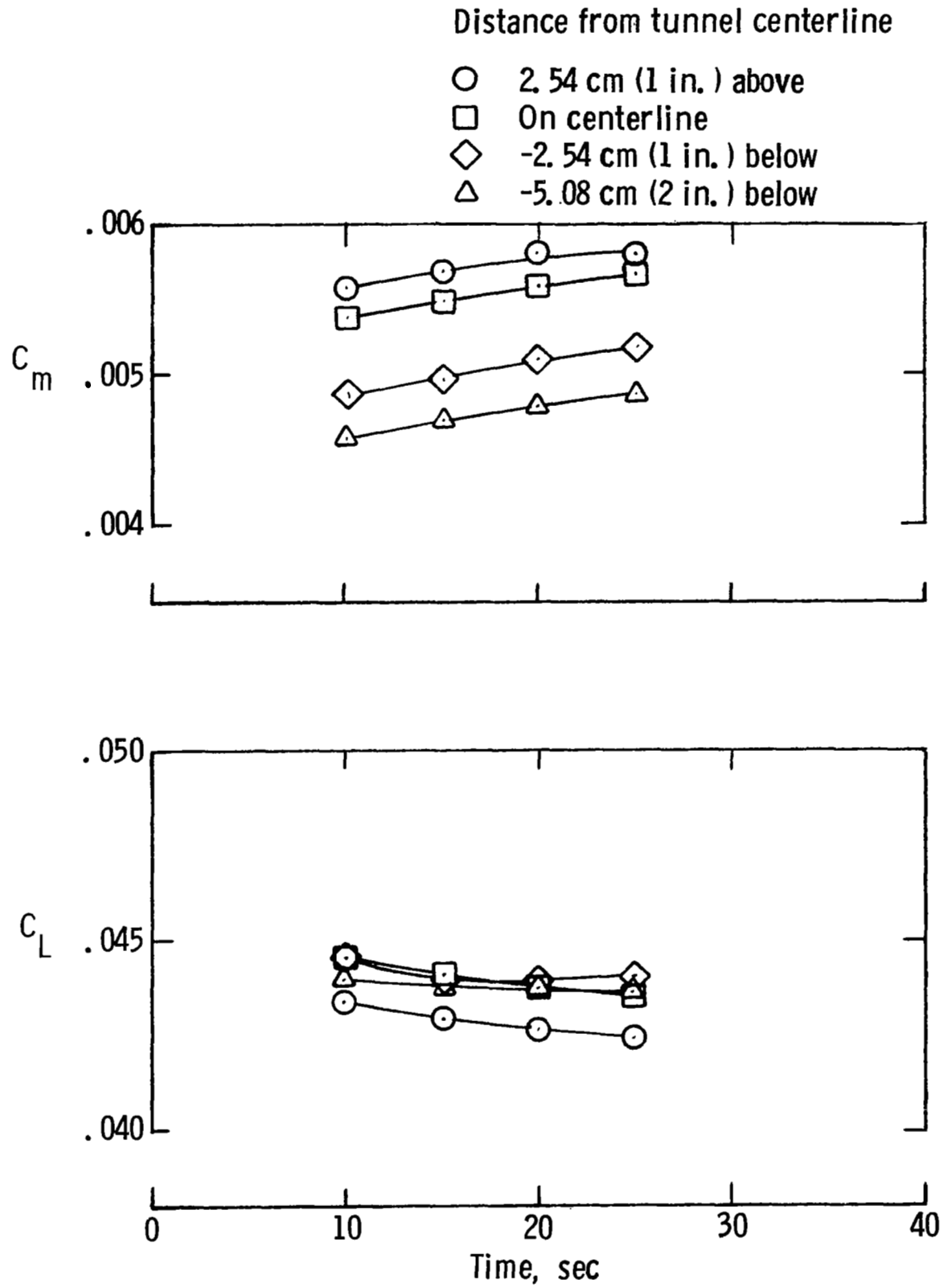

Figure 22.- Variation of lift and pitching-moment coefficients with blowdown-tunnel test time for various vertical test-section locations in the Langley Mach 8 Variable-Density Tunnel. $R_l = 11.01 \times 10^6$; $\alpha = 3°$.

1. Report No.	2. Government Accession No.	3. Recipient's Catalog No.
NASA TP-2159		

4. Title and Subtitle	5. Report Date
WALL-TEMPERATURE EFFECTS ON THE AERODYNAMICS OF A HYDROGEN-FUELED TRANSPORT CONCEPT IN MACH 8 BLOWDOWN AND SHOCK TUNNELS	July 1983
	6. Performing Organization Code: 505-31-73-01
7. Author(s): Jim A. Penland, Don C. Marcum, Jr., and Sharon H. Stack	8. Performing Organization Report No.: L-15100
	10. Work Unit No.
9. Performing Organization Name and Address: NASA Langley Research Center, Hampton, VA 23665	11. Contract or Grant No.
	13. Type of Report and Period Covered: Technical Paper
12. Sponsoring Agency Name and Address: National Aeronautics and Space Administration, Washington, DC 20546	14. Sponsoring Agency Code

15. Supplementary Notes

16. Abstract

Results are presented from two separate tests on the same blended wing-body hydrogen-fueled transport model at a Mach number of about 8 and a range of Reynolds numbers (based on theoretical body length) of 0.597×10^6 to about 156.22×10^6. Tests were made in a conventional hypersonic blowdown tunnel and a hypersonic shock tunnel at angles of attack of -2° to about 8°, with an extensive study made at a constant angle of attack of 3°. The model boundary-layer flow varied from laminar at the lower Reynolds numbers to predominantly turbulent at the higher Reynolds numbers. Model wall temperatures and stream static temperatures varied widely between the two tests, particularly at the lower Reynolds numbers. These temperature differences resulted in marked variations of the axial-force coefficients between the two tests, due in part to the effects of induced pressure and viscous interaction variations. The normal-force coefficient was essentially independent of Reynolds number. Analysis of results utilized current theoretical computer programs and basic boundary-layer theory.

17. Key Words (Suggested by Author(s))	18. Distribution Statement
Laminar skin friction Turbulent skin friction Boundary-layer induced pressure Hypersonic aircraft Computational aerodynamics	Unclassified - Unlimited Subject Category 02

19. Security Classif. (of this report)	20. Security Classif. (of this page)	21. No. of Pages	22. Price
Unclassified	Unclassified	59	A04

For sale by the National Technical Information Service, Springfield, Virginia 22161

NASA-Langley, 1983

3 1 1U,A, 830725 S00903DS
DEPT OF THE AIR FORCE
AF WEAPONS LABORATORY
ATTN: TECHNICAL LIBRARY (SUL)
KIRTLAND AFB NM 87117

S